Ocean Engineering 91 (2014) 28–50

Contents lists available at ScienceDirect

Ocean Engineering

journal homepage: www.elsevier.com/locate/oceaneng

Numerical analysis on springing and whipping using fully-coupled FSI models

Jung-Hyun Kim, Yonghwan Kim *

Department of Naval Architecture & Ocean Engineering, Seoul National University, 1, Gwanak-ro, Gwanak-gu, Seoul 151-744, Republic of Korea

ARTICLE INFO

Article history:
Received 18 September 2013
Accepted 4 August 2014
Available online 16 September 2014

Keywords:
Hydroelasticity
Springing
Whipping
Rankine panel method
Fluid–structure interaction (FSI)

ABSTRACT

This paper focuses on ship springing and whipping analysis using a three-dimensional (3-D) Rankine panel method combined with a beam-element-based 1-D structural model and a shell-element-based 3-D structural model. In addition, slamming loads are considered by 2-D generalized Wagner model (GWM). The beam model is a classical idealization of a ship structure, which is based on Timoshenko beam theory for bending and Vlasov beam theory for non-uniform torsion. The 3-D model consists of beam and shell elements, and its motions are approximated by a few of lower modes. Different coupling schemes are applied to couple the 3-D panel method and the different structure models. Whereas the 1-D beam model is coupled in a Cartesian coordinate system, the 3-D finite element (FE) model is coupled in a generalized coordinate system. The difference in coordinate systems leads to different numerical implementations of coupling. Agreement and discrepancy between the coupled models are discussed regarding results for a 60 m barge, a 6500 TEU containership, and an experimental model of a virtual 10,000 TEU containership. The bulkheads in the barge and the 6500 TEU containership are properly considered in beam modeling according to relative stiffness between the bulkheads and hulls. In linear responses to waves, good agreement is obtained between all the models. However, differences between the models are found in nonlinear springing and whipping responses.

1. Introduction

Wave-induced vibration referred to springing and whipping can cause critical problems in a fatigue design of larger and faster merchant ships. It is well known that the problem is due to decreasing natural frequency and increasing forward speed. Particularly, the size of containerships has drastically increased in the past 5–6 years, and it is still increasing. The fatigue damage induced by springing and whipping can be a major contributor to total fatigue damage for the larger containerships. Many numerical simulations, experiments and full scale measurements have been carried out, and the importance of springing and whipping has been revealed (Storhaug, 2007; Drummen et al., 2008).

The representative early attempt to numerically simulate springing was done by Bishop and Price (1979). A combination of Timoshenko beam and linear strip theory is quite practical and has a potential for more sophisticated methods. Timoshenko beam theory does not cover non-uniform torsion and structural discontinuity, but they can play a role in the torsional responses of containerships. Senjanović et al. (2009a) successfully considered them in the analysis of containerships based on the thin-walled girder theory. A direct way to consider them is to model the whole structure using 3-D FEM. This is rather simple compared to using the sophisticated beam theory in conjunction with consideration of structural discontinuity. Successful applications of 3-D FE model in hydroelastic analysis based on modal approach are found in the recent papers (Hirdaris et al., 2003; Malenica and Tuitman, 2008; Iijima et al., 2008). Recently, 3-D FEM is directly coupled with 3-D Rankine panel method in time domain by Kim et al. (2013).

In the fluid domain, meanwhile, various numerical models have been proposed. For example, a second-order strip, a 3-D potential theory with a weakly nonlinear approach, and a Reynolds Averaged Navier–Stokes (RANS) model have been applied to springing analysis (Jensen and Dogliani, 1996; Oberhagemann and Moctar, 2011). The significant trend is to consider nonlinear excitation due to the fact that nonlinear springing can be important as well as linear springing. A body nonlinearity may be one of the significant sources of nonlinear springing. Up to now, the 3-D potential theory with the weakly nonlinear approach is thought to be the most practical method for the fluid domain. In the future, nonlinear free surface body interactions should be solved for nonlinear springing analysis (Shao and Faltinsen, 2010). For consideration of slamming loads, 2-D methods are commonly used because 3-D method requires complicated treatment and heavy computational burden compared to the linear panel method of 3-D potential flow.

* Corresponding author. Tel.: +82 2 880 1543; fax: +82 2 876 9226.
E-mail addresses: wowplusme@snu.ac.kr (J.-H. Kim), yhwankim@snu.ac.kr (Y. Kim).

http://dx.doi.org/10.1016/j.oceaneng.2014.08.001

Nomenclature

a	thickness of bulkhead
$\overrightarrow{A}^j$	cross-section area
$\overrightarrow{A}^{j,k}$	eigenvector of jth mode
$\delta\overrightarrow{A}_i$	eigenvector variation of jth mode due to unit displacement of kth mode
α	integration parameter of Newmark-Beta method
$b(t)$	instantaneously submerged breadth
$B_j(\overrightarrow{x})$	bi-quadratic spline function
β	heading angle of incident wave
$c(t)$	intersection point
C	Rayleigh damping matrix
C_S	structural stiffness of natural mode
C_R	fluid restoring
C	energy coefficient of bulkhead
$\overrightarrow{c}^j$	coefficient vector for gravity force
χ	integration parameter of Newmark-Beta method
D	draft of each slamming section
$\overrightarrow{\delta}$	translational displacement vector on the body surface
E	Young's modulus
ε	value much smaller than 1
ε_x	normal strain in x-direction
ε_y	normal strain in y-direction
f^j_{SP}	soft spring force of jth mode
f^j_{DAM}	damping force of jth mode
f^j_{LD}	linear part of dynamic force of jth mode
f^j_{NF}	nonlinear Froude–Krylov force of jth mode
f^j_{NR}	nonlinear restoring force of jth mode
f^j_{SL}	slamming force of jth mode
f^j_{LT}	total linear dynamic force of jth mode
f_G	gravity force
f_{IN}	inertial force
f^j_{sf}	sectional force (j=1–3 denote axial and shear forces, j=4–6 moments)
$f^j(t)$	external force of jth mode
$f(x)$	body geometry
$f'(x)$	slope of body geometry
$\overrightarrow{f}$	external forcing vector
F_x	axial force
F_y	horizontal shear force
F_z	vertical shear force
$F_\infty(c)$	coefficient in the far field asymptotic of the conformal mapping
$\delta F^{j,k}_R$	restoring force of jth mode due to unit displacement of kth mode
g	gravity constant
$\overrightarrow{g}$	gravity acceleration vector
γ	dead-rise angle
γ_{xy}	shear strain in x–y plane
$\dot{h}$	relative velocity
$\ddot{h}$	relative acceleration
$H(t)$	free surface elevation in GWM
I_t	torsional modulus
$I_t{}^*$	modified torsional modulus
I_w	warping constant
I_y	second moment of area with respect to y-axis
I_z	second moment of area with respect to z-axis
k	wave number
K	restoring matrix
K_D	restoring matrix for dynamic analysis
K_Q	restoring matrix for quasi-static analysis
$K_{QD,DQ}$	cross-coupling restoring matrix of dynamic and quasi-static analyses
K_y	effective shear factor in y-direction
K_y	effective shear factor in z-direction
κ	damping strength
L	ship length
l_0	distance between the centers of adjacent bulkheads
l_1	distance between adjacent bulkheads ($=l_0-a$)
m_i	nodal mass of ith node
M	mass matrix
$\hat{\mathrm{M}}$	6×6 mass matrix of node
$M(\infty)$	infinite frequency added mass matrix
M_D	mass matrix for dynamic analysis
M_Q	mass matrix for quasi-static analysis
M_a	added mass
M_x	torsional moment
M_y	vertical bending moment
M_z	horizontal bending moment
n	number of flexible modes in the coupled-analysis
n_n	total number of nodes
n_p	total number of panels
$\overrightarrow{n}$	normal vector on the body surface
$\delta\overrightarrow{n}^k_i$	normal vector variation due to unit displacement of kth mode
$N(c)$	functions from Wagner equation
ν	Poisson's ratio
ω	wave frequency
ω_e	encounter frequency
ω_i	natural frequency of ith mode in dry mode
ω_{bn}	natural frequency of 2-node vertical bending in wet mode
ω_{tn}	natural frequency of 2-node torsion in wet mode
p	total fluid pressure
p_i	static pressure on ith panel
δp^k_i	static pressure variation on ith panel due to unit displacement of kth mode
p_{LD}	linear part of dynamic pressure
p_{LT}	total linear dynamic pressure
p_{NF}	nonlinear Froude–Krylov pressure
p_{NR}	nonlinear restoring pressure
p_{GWM}	GWM pressure
ϕ	total velocity potential
Φ	double-body basis potential
ϕ_I	incident wave potential
ϕ_d	disturbed wave potential
φ	velocity potential in GWM
ρ	fluid density
$\overrightarrow{s}^j$	the coefficient vector for sectional force calculation
S_i	area of ith panel
S_{SL}	slamming section surface
$S(x,t)$	vertical velocity of free surface
S_B	exact body surface
$\overline{S}_B$	mean body surface
σ_x	normal stress in x-direction
σ_y	normal stress in y-direction
$\sigma_x{}^j$	normal stress in x-direction of jth mode
Ω_F	fluid domain
t	plate thickness
t	time
Δt	time step size
τ_{xy}	shear stress in x–y plane
$\partial\theta/\partial x$	derivative of rotation around x-axis with respect to x

$u_x^n(t)$	x-displacement at the neutral axis	$\vec{x}$	position vector
$u_y^s(t)$	y-displacement at the shear center	$X_c(\xi,c)$	function from conformal mapping
$\vec{u}_g(t)$	effective displacement vector for gravity	ξ	x-coordinate on the wetted body surface normalized by $c(t)$
$\vec{u}$	equivalent nodal acceleration vector	ξ^j	modal displacement of jth mode in generalized coordinate system
$\vec{u}$	nodal displacement vector in Cartesian coordinate system	$\dot{\xi}^j$	modal velocity of jth mode in generalized coordinate system
$\dot{\vec{u}}$	nodal velocity vector in Cartesian coordinate system	$\ddot{\xi}^j$	modal acceleration of jth mode
$\ddot{\vec{u}}$	nodal acceleration vector in Cartesian coordinate system	$\xi_{,j}$	equivalent modal acceleration of jth mode
$\vec{U}$	ship forward speed vector	ζ	total wave elevation
U	magnitude of ship forward speed	ζ_I	incident wave elevation
$w_{1,2,3}$	weight function of node	ζ_d	disturbed wave elevation
x_p	x-coordinate of sectional force evaluation		

This paper presents three different structure models, which are combined with the B-spline 3-D Rankine panel method. Many WISH program families are based on the method (Kim et al., 2011). The three models are (1) the beam theory model, (2) the modified beam model based on the 3-D FE model, and (3) the 3-D FE model. Characteristics of the models are discussed regarding the results for a 60 m barge, a 6500 TEU containership, and an experimental model of a virtual 10,000 TEU containership. A similar study is found in the work of Hirdaris et al. (2003). However, the present study couples fluid and structure models in the time domain and also simulates nonlinear springing and whipping.t

2. Mathematical background

2.1. Fluid domain

The fluid motion surrounding a ship structure is solved by a numerical method based on a 3-D potential theory. The method in this study follows the works of Nakos (1990), Kring (1994) and Kim and Kim (2008). Let us consider a Cartesian coordinate system with its origin on mean water level as shown in Fig. 1. It moves with the advance of the ship with forward speed along the x-axis. The origin is located on the mass center projected on the water plane. The irrotational flow of inviscid and incompressible fluid is assumed, and the governing equation of the fluid motion reduces to the Laplace equation. The set of the boundary value problem is expressed as

$$\nabla^2\phi = 0 \quad \text{in } \Omega_F \tag{1}$$

$$\frac{\partial\phi}{\partial n} = \vec{U}\cdot\vec{n} + \frac{\partial\vec{u}}{\partial t}\cdot\vec{n} \quad \text{on } S_B \tag{2}$$

$$\left[\frac{d}{dt} + \nabla\phi\cdot\nabla\right][z-\zeta(x,\,y,\,t)] = 0 \quad \text{on } z=\zeta(x,\,y,\,t) \tag{3}$$

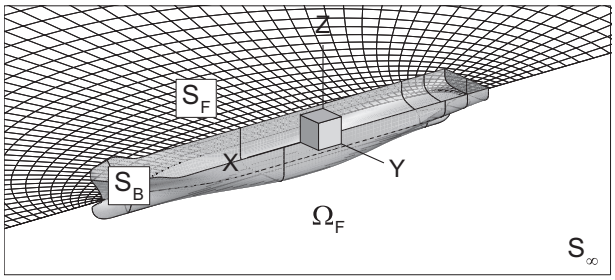

Fig. 1. Coordinate system and notation.

$$\frac{d\phi}{dt} = -g\zeta - \tfrac{1}{2}\nabla\phi\cdot\nabla\phi \quad \text{on } z=\zeta(x,\,y,\,t) \tag{4}$$

where $d/dt = \partial/\partial t - \vec{U}\cdot\nabla$ is Galilean transformation.

In order to linearize the boundary conditions of Eqs. (2)–(4), the velocity potential is decomposed into the double-body basis potential, the incident potential, and the disturbed potential. By the same manner, the free surface elevation is also decomposed into the incident wave elevation and the disturbed wave elevation.

$$\phi(\vec{x},\,t) = \Phi(\vec{x}) + \phi_I(\vec{x},\,t) + \phi_d(\vec{x},\,t) \tag{5}$$

$$\zeta(\vec{x},\,t) = \zeta_I(\vec{x},\,t) + \zeta_d(\vec{x},\,t) \tag{6}$$

Double-body linearization assumes that the basis potential is order of 1, and the other potentials are order of ε (Dawson, 1977). Each wave elevation is order of ε. The disturbed potential and wave elevation include both steady and unsteady potentials and wave elevations, respectively. The free surface boundary conditions are linearized using Taylor series expansion about the calm water level ($z=0$). At first, Eqs. (5) and (6) are substituted to Eqs. (3) and (4). Next, Taylor expanding of the equations about $z=0$ is applied. Finally, terms of order higher than ε are dropped. The final form of the free surface boundary conditions are expressed as (Kim and Kim, 2008)

$$\frac{\partial\zeta_d}{\partial t} - (\vec{U}-\nabla\Phi)\cdot\nabla\zeta_d = \frac{\partial^2\Phi}{\partial z^2}\zeta_d + \frac{\partial\phi_d}{\partial z} + (\vec{U}-\nabla\Phi)\cdot\nabla\zeta_I \quad \text{on } z=0 \tag{7}$$

$$\frac{\partial\phi_d}{\partial t} - (\vec{U}-\nabla\Phi)\cdot\nabla\phi_d = -\frac{\partial\Phi}{\partial t} - g\zeta_d + \left[\vec{U}\cdot\nabla\Phi - \frac{1}{2}\nabla\Phi\cdot\nabla\Phi\right] + (\vec{U}-\nabla\Phi)\cdot\nabla\phi_I \quad \text{on } z=0 \tag{8}$$

The body boundary condition is linearized by Taylor series expansion about the mean body surface as (Timman and Newman, 1962)

$$\frac{\partial\phi_d}{\partial n} = [(\vec{u}\cdot\nabla)(\vec{U}-\nabla\Phi) + ((\vec{U}-\nabla\Phi)\cdot\nabla)\vec{u}]\cdot\vec{n} + \frac{\partial\vec{u}}{\partial t}\cdot\vec{n} - \frac{\partial\phi_I}{\partial n} \quad \text{on } \bar{S}_B \tag{9}$$

The form of Ogilvie and Tuck (1969) is extended to flexible modes using eigenvectors as

$$\frac{\partial\phi_d}{\partial n} = \sum_{j=1}^{6+n}\left(\frac{\partial\xi_j}{\partial t}n_j + \xi_j m_j\right) - \frac{\partial\phi_I}{\partial n} \quad \text{on } \bar{S}_B \tag{10}$$

$$n_j = \vec{A}_j\cdot\vec{n}$$

$$m_j = (\vec{n}\cdot\nabla)(\vec{A}^j\cdot(\vec{U}-\nabla\Phi)) \tag{11}$$

where superscript j indicates rigid body motions (1∼6) or flexible motions (7∼).

If it is assumed that Rankine sources are distributed on the free and body surfaces, the volume integral of the Laplace equation is converted to the boundary integral by Green's second identity.

$$\phi_d + \iint_{S_B} \phi_d \frac{\partial G}{\partial n} dS - \iint_{S_F} \frac{\partial \phi_d}{\partial n} G dS = \iint_{S_B} \frac{\partial \phi_d}{\partial n} G dS - \iint_{S_F} \phi_d \frac{\partial G}{\partial n} dS \tag{12}$$

This equation is numerically solved by spatial and temporal discretization in the time domain. The boundaries to be discretized are limited to the mean body surfaces and the free surface near the body. The radiation condition is satisfied on the edges of the free surface using artificial damping zone. In the damping zone, the wave elevation and potential are damped as follows (Kring, 1994):

$$\frac{d\zeta_d}{dt} = \frac{\partial \phi_d}{\partial z} - 2\kappa\zeta_d + \frac{\kappa^2}{g}\phi_d$$
$$\frac{\partial \phi_d}{\partial t} = -g\zeta_d \tag{13}$$

If the damping zone size is not enough or the damping strength is too high, the radiated wave returns to the body and pollutes the solution.

Once the velocity potential is obtained by solving the boundary value problem, the linear total dynamic pressure on the body surface is obtained by Bernoulli equation as

$$p_{LT} = -\rho\left\{\left(\frac{\partial}{\partial t} - \overline{U}\cdot\nabla\right)(\Phi + \phi_I + \phi_d) + \nabla\Phi\cdot\nabla\left(\frac{1}{2}\Phi + \phi_I + \phi_d\right)\right\} \tag{14}$$

In linear computation, the pressure is integrated over the mean wetted surface.

In order to consider a nonlinear fluid pressure, a nonlinear boundary value problem should be solved, but it is very complicated and time-consuming in a 3-D space. In the present study, a weakly nonlinear approach is adopted to take into account the nonlinear Froude–Krylov and restoring pressures due to body geometry. The weakly nonlinear approach is inconsistent but effective to reduce computational cost because nonlinear radiation and diffraction forces are missing. The nonlinear Froude–Krylov pressure is calculated by Taylor expanding of the incident wave potential about the calm water level as follows:

$$z < 0 \quad \phi_I = \frac{gA}{\omega} e^{kz} \sin(k(x + Ut)\cos\beta + ky\sin\beta - \omega t)$$
$$0 < z < \zeta_I \quad \phi_I = \frac{gA}{\omega} \sin(k(x + Ut)\cos\beta + ky\sin\beta - \omega t) \tag{15}$$

$$p_{NF} = -\rho\left\{\left(\frac{\partial}{\partial t} - \overline{U}\cdot\nabla\right)\phi_I + \nabla\Phi\cdot\nabla\phi_I + \frac{1}{2}\nabla\phi_I\cdot\nabla\phi_I\right\} \tag{16}$$

The nonlinear Froude–Krylov pressure works with an extension of restoring pressure, which is negative above the calm water level. The nonlinear pressure is integrated over the instantaneously wetted surface.

The linear part of the dynamic pressure is obtained by dropping the terms related with the incident wave potential from Eq. (14) as

$$p_{LD} = -\rho\left\{\left(\frac{\partial}{\partial t} - \overline{U}\cdot\nabla\right)(\Phi + \phi_d) + \nabla\Phi\cdot\nabla\left(\frac{1}{2}\Phi + \phi_d\right)\right\} \tag{17}$$

The linear part is integrated over the mean body surface.

2.2. Symmetric slamming model

For calculation of slamming forces, the ship is discretized into 2-D sections along the longitudinal axis, which covers the whole ship from stern to bow. The sections are perpendicular to the free surface of the calm water in Fig. 2. Longitudinal mesh for each section is used to integrate slamming loads. Symmetric slamming forces acting on the sections are considered by either wedge approximation or GWM. Only water entry problem is considered. Asymmetric slamming forces for torsion and horizontal bending are not considered. Wedge approximation is based on momentum conservation, which is expressed as

$$F = \frac{d}{dt} M_a \dot{h} = M_a \ddot{h} + \frac{\partial M_a}{\partial t}\dot{h} \tag{18}$$

The relative displacement and velocity are calculated as follows:

$$\dot{h} = -\frac{\partial \vec{u}}{\partial t}\cdot(0,\ 0,\ 1) + \frac{\partial \zeta_I}{\partial t} \tag{19}$$

$$h = -\vec{u}\cdot(0,\ 0,\ 1) + \zeta_I + D \tag{20}$$

Wedge approximation follows von Karman's solution with simplified wedge shapes. Once the surrounding flow is assumed as a potential flow, the infinite frequency added mass of the wedge is calculated as

$$M_a = \frac{\pi}{2}\rho b^2(t)\left(1 - \frac{\gamma}{2\pi}\right) \tag{21}$$

In case of GWM, the body geometry enters water with a vertical velocity shown in Fig. 3. Slamming pressure is limited to the water entry problem without flow separation. The space-fixed coordinate system is used, the origin of which is located at the intersection of the vertical axis of symmetry and the free surface of the calm water. The set of the initial value problem is expressed as follows (Zhao and Faltinsen, 1993; Korobkin, 2010; Khabakhpasheva et al., 2014):

$$\nabla^2\varphi = 0 \tag{22}$$

$$\varphi = 0 \quad (y = H(t)) \tag{23}$$

$$S(x,\ t) = \varphi_y(x,\ H(t),\ t) \quad (|x| > c(t)) \tag{24}$$

$$\varphi_y = f'(x)\varphi_x - \dot{h}(t) \quad (y = f(x) - h(t), \quad |x| < c(t)) \tag{25}$$

$$\varphi \to 0 \quad (x^2 + y^2 \to \infty) \tag{26}$$

$$H(t) = f(c(t)) - h(t) \tag{27}$$

$$S(x,\ 0) = 0, \quad c(0) = 0 \tag{28}$$

The initial boundary value problem is solved using a conformal mapping technique. The final form of the pressure is obtained by Bernoulli equation as follows:

$$p_{GWM} = \rho\dot{h}^2 P_v(\xi,\ c) + \rho\ddot{h} P_w(\xi,\ c) \tag{29}$$

$$P_v(\xi, c) = \frac{X_c(\xi, c)}{N(c)}\frac{\xi}{S(\xi, c)}(1 - \xi)^{-k(c)} - \frac{0.5}{1 + f_x^2(X)}\frac{\xi^2}{S^2(\xi, c)}(1 - \xi)^{-2k(c)} + \frac{F'_\infty(c)}{N(c)}\sqrt{1 - \xi^2} + \frac{1}{2} - \frac{f_x(c)}{N(c)} \tag{30}$$

$$P_w(\xi, c) = f(X) - f(c) + F_\infty(c)\sqrt{1 - \xi^2} \tag{31}$$

The derivation of the pressure is mathematically complicated. The details about the solution were introduced by Khabakhpasheva et al. (2014).

The final form of the pressure explicitly guarantees that the pressure is not dependent on the time histories of the body motion but on the current velocity and acceleration. Thus, if a pressure distribution is obtained with the zero initial condition which means that the body starts to enter the water from a non-submerged condition, it can be used to other water entry problems with non-zero initial conditions. It can be achieved by setting offset values in the splash-up of the free surface.

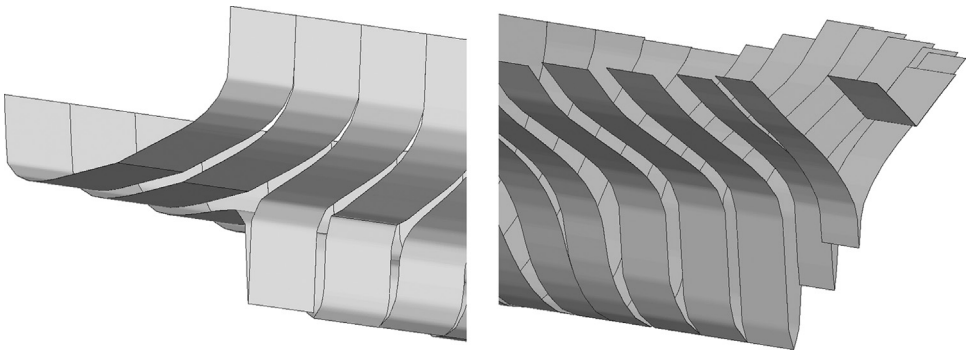

Fig. 2. Slamming sections for evaluation of slamming pressure (left: stern, right: bow).

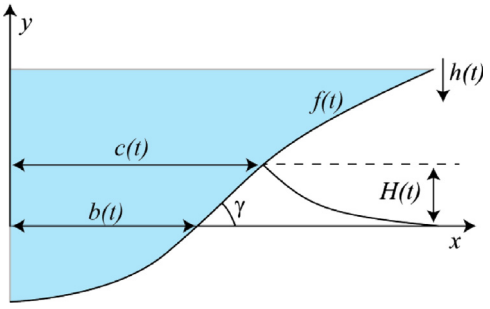

Fig. 3. Definitions for slamming cross-section.

In time-marching simulation, generally, it is needed to take a small time step for GWM. In this study, however, it is not needed because a contact point is discretized instead of time (Khabakhpasheva et al., 2014). The contact point grows from zero to the maximum breadth. For each discretized contact point, pressure distribution is calculated. Linear interpolation is used to obtain pressure distribution when a contact point is located between two discretized contact points. Therefore, the time step size do not need to be small.

A major difference between the two models is consideration of a free surface elevation due to a water entry. GWM will calculate shorter impact duration compared to that of wedge approximation. It can leads to higher whipping responses by GWM compared to those by wedge approximation because impact duration is not much shorter than a natural period of 2-node vertical bending for large containerships.

Generally, 2-D method overestimates slamming forces because no flow is considered in the longitudinal direction. Especially, it calculates higher slamming forces near stern and bow compared to those of 3-D method. However, relaxation coefficients are not considered in this study because a thorough comparison between 2-D and 3-D results is needed. In the future, the 3-D effect and relaxation coefficients will be discussed.

2.3. Beam theory approximation

Ship structures have been modeled as beams for a long time. Timoshenko beam theory gives good approximated solutions to bending problems (Bishop and Price, 1979). However, ship structures with large openings on the deck are frequently exposed to torsional springing because they have very low torsional rigidity due to a large warping distortion. To consider warping-dominant torsion, Vlasov beam theory is adopted (Gjelsvik, 1981). Timoshenko and Vlasov beam theories are quite sophisticated, and they require 2-D analysis of cross-sections for the effective shear factor, torsional modulus, and warping modulus. In addition, structural discontinuity due to bulkheads or openings in the deck should be considered properly. The beam approximation is coupled with the 3-D Rankine panel method in a Cartesian coordinate system. A springing analysis program based on this coupled method, WISH-FLEX BEAM, has been developed by the WISH-FLEX Joint Industry Project (WISH-FLEX JIP) at Seoul National University (Kim et al., 2011).

In this part, the coupling method is briefly described without any figures and equations. The details were introduced by the works of Kim et al. (2009a, 2009b, 2009c). It should be noted that the beam and the fluid panel modes are coupled based on nodal motions in the Cartesian coordinate system. Most fluid–structure coupling has been performed in a generalized coordinate system. Handling of the so-called *m*-term and restoring force in the node-based coupling is different from that in mode-based coupling. For example, the fluid restoring force is composed of pressure, normal vector, and mode variations in a generalized coordinate system (Senjanović et al., 2008). Their contributions depend on the wetted hull surface. In general, pressure variation is predominant, and mode variation has the smallest portion. Pressure and normal vector variations in the Cartesian coordinate system have the similar form as those in the generalized coordinate system, but mode variation has a different form in the Cartesian coordinate system, which corresponds to geometric stiffness. It can be understood as moment arm variation. Moment arm variation is missing in the current state of the nodal-based coupled method. Explicit expressions for restoring force in both Cartesian and generalized coordinate systems were discussed in the work of Senjanović et al. (2013).

In the coupling of the 3-D Rankine panel model, 2-D slamming model, and the beam model, it is essential to exchange the motion and pressure between the models. The dynamic, static, and slamming pressures are distributed to two adjacent nodes as nodal force using shape function of beam element. The motions of the body surface and slamming sections are calculated by motions of the two adjacent node and the shape function. The details follow the works of Kim et al. (2009a, 2009b, 2009c).

2.4. Modified beam approximation

A modified beam model is proposed to utilize eigenvectors of the 3-D FE model in the beam theory model when modal superposition method is used. It is a hybrid model in transition from beam theory model to 3-D FE model. The purpose is to confirm whether the hybrid model has both advantages of the fast computation speed of beam model and the accuracy of 3-D FE model or not.

The model approximates a ship structure as a beam, but beam theory is not used because the eigenvectors at beam nodes are obtained from the 3-D FE model using linear interpolation. Eigenvalue analysis of the 3-D FE model can be performed by commercial FEM software.

It should be noted that stiffness and mass matrices of the beam element are not formulated, but the inertial properties of the 3-D FE model are modeled by lumped mass distribution along the longitudinal axis for gravity restoring and sectional force calculation.

The advantages of the hybrid model can be the simplicity of the underlying theory, the accuracy of the 3-D FE model, and the low computation cost of the beam model. However, the lumped mass modeling makes the model inconsistent. If the differences in the inertial properties between the shell 3-D model and the lumped mass distribution are small, the inconsistency will be negligible. The hybrid model is implemented in WISH-FLEX BEAM and is named WISH-FLEX BEAM+3-D FEM in the results.

2.5. 3-D FE model

This section describes how to couple the fluid models with the 3-D FE model via eigenvectors. There are three topics, which are approximated equation of motion in generalized coordinate system, recalculation of eigenvectors on the panel model using linear interpolation, and external forces. The use of the 3-D FE model is very straightforward for overcoming the disadvantages of the beam theory. Moreover, it is rather simple compared to the sophisticated beam theory conjunction with 2-D analysis of cross-section and consideration for structural discontinuity. However, large degrees of freedom (DOF) should be reduced by modal superposition method in time-domain simulations. There are two assumptions for DOF reduction by modal superposition method. Firstly, motion on the body surface easily converges with a few lower modes because modal stiffness rapidly increases in higher modes except for local modes. It is negligible, the fluid disturbance, due to motions of higher modes. Secondly, responses of higher modes are quasi-static. According to the first assumption, the displacement vector field in Cartesian coordinate system can be expressed as

$$\vec{u}(t)=\sum_{j=1}^{6*m}\xi^j(t)\vec{A}^j\approx\sum_{j=1}^{6+n}\xi^j(t)\vec{A}^j=[\vec{A}^1\vec{A}^2\cdots\vec{A}^{6+n}]\{\xi^{1\sim 6+n}(t)\} \tag{32}$$

where n is typically smaller than 20.

According to the second assumption, the original form of equation of motion can be expressed as

$$\begin{bmatrix}M_D & 0\\ 0 & M_Q\end{bmatrix}\begin{Bmatrix}\ddot{\xi}^{1\sim 6+n}(t)\\ \ddot{\xi}^{7+n\sim}(t)\end{Bmatrix}+\begin{bmatrix}K_D & K_{DQ}\\ K_{QD} & K_Q\end{bmatrix}\begin{Bmatrix}\xi^{1\sim 6+n}(t)\\ \xi^{7+n\sim}(t)\end{Bmatrix}=\{f^{1\sim}(t)\} \tag{33}$$

The mass matrix consists of only diagonal terms of 1 except the rigid body part of 6×6. The rigid body part is defined at the mass center projected on the free surface of the calm water. By applying the two assumptions to Eq. (33) for DOF reduction, it reduces to

$$M_D\{\ddot{\xi}^{1\sim 6+n}(t)\}+K_D\{\xi^{1\sim 6+n}(t)\}=\{f^{1\sim 6+n}(t)\} \tag{34}$$

Eq. (34) will be solved to obtain modal responses in the coupled-analysis. The response includes both dynamic and quasi-static components. The linear restoring matrix consists of structural stiffness of natural mode and fluid restoring. Gravity restoring is also included in the fluid restoring. It is expressed as

$$K_D=C_S+C_R$$

$$C_S^{i,j}=\omega_i{}^2\quad(i=j\ \text{and}\ i,j>6),\quad C_S^{i,j}=0 \tag{35}$$

In addition, quasi-static responses of higher modes can be obtained by solving the decoupled equation as

$$K_Q\{\xi^{7+n\sim}(t)\}=[(\vec{A}^{7+n\sim})^T]\{f^{7+n\sim}(t)\}-K_{QD}\{\xi^{1\sim 6+n}(t)\} \tag{36}$$

In this study, Eq. (36) will not be solved. However, contributions of all modes to sectional force can be considered by direct integration of all external and inertial forces. It will be discussed in Section 3.5.

The 3-D FE model is coupled with the 3-D Rankine panel method via eigenvectors. If the panel method and FEM share the same structure model, eigenvectors of the structure can be used in the panel method directly. In most cases, however, eigenvectors should be recalculated on the panel model grid because different grids are preferred in the panel method and eigenvalue analysis. The present study recalculates eigenvectors on the grid of the panel model using linear interpolation.

Eigenvectors are recalculated on the center of panel as follows. The first step is to find a tri or quad element which is the nearest to the center of panel shown in Fig. 4. Next, following equations are derived if the center of the panel is located on the surface of the element:

$$(x_p,\ y_p,\ z_p)=w_1(x_{n1},\ y_{n1},\ z_{n1})+w_2(x_{n2},\ y_{n2},\ z_{n2})+w_3(x_{n3},\ y_{n3},\ z_{n3}) \tag{37}$$

$$\vec{A}^j(x_p,\ y_p,\ z_p)=w_1\vec{A}^j(x_{n1},\ y_{n1},\ z_{n1})+w_2\vec{A}^j(x_{n2},\ y_{n2},\ z_{n2})+w_3\vec{A}^j(x_{n3},\ y_{n3},\ z_{n3}) \tag{38}$$

The weight functions are obtained by solving Eq. (37). If the matrix of the three position vectors in Eq. (37) is singular, the all four vectors in Eq. (37) should be slightly translated in x, y or z direction. Finally, the eigenvector on the center of the panel is recalculated by Eq. (38). Fig. 5 shows an example of recalculated eigenvector on a fine mesh panels. The eigenvectors are also recalculated on meshes of slamming sections.

Fluid restoring should be differently defined in linear and weakly nonlinear computations. Linear restoring matrix is defined in discretized form as follows:

$$C_R=\begin{bmatrix}\delta F_R^{1,1} & \cdots & \delta F_R^{1,m}\\ \vdots & \ddots & \vdots\\ \delta F_R^{m,1} & \cdots & \delta F_R^{m,m}\end{bmatrix} \tag{39}$$

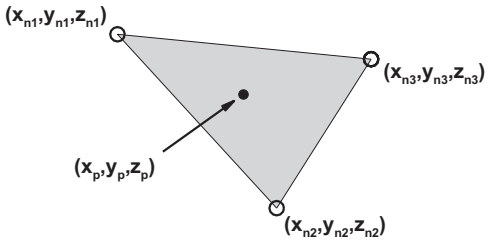

Fig. 4. The nearest element to the center of panel.

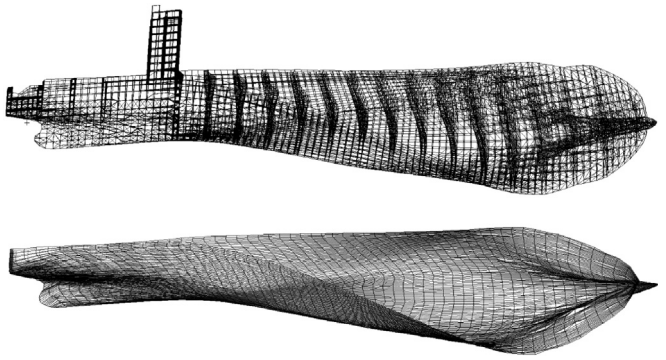

Fig. 5. Linear interpolation of eigenvector: the 3-D FE model (upper) and the panel model (bottom).

$$\delta F_{R.}^{j,k} = \sum_{i=1}^{n_p} \{(p_i+\delta p_i^k)(S_i+\delta S_i^k)(\vec{n}_i+\delta\vec{n}_i^{\,k})\cdot(\vec{A}_i^{\,j}+\delta\vec{A}_i^{\,j,k}) - p_i S_i \vec{n}_i \cdot \vec{A}_i^{\,j}\}$$

$$+ \sum_{i=1}^{n_n} (m_i(\vec{A}_i^{\,j}+\delta\vec{A}_i^{\,j,k})\cdot\vec{g} - m_i\vec{A}_i^{\,j}\cdot\vec{g}) \quad (40)$$

The last term is not fluid restoring but gravity restoring. It is assumed that δp_i^k, $\delta\vec{n}_i^{\,k}$, and $\delta\vec{A}_i^{\,j,k}$ are order of ε, δS_i^k is much smaller than ε, and the others are order of 1. The final form is obtained by dropping terms of order higher than ε as

$$\delta F_{R.}^{j,k} = \sum_{i=1}^{n_p} \{\delta p_i^k S_i \vec{n}_i \cdot \vec{A}_i^{\,j} + p_i S_i \delta\vec{n}_i^{\,k}\cdot\vec{A}_i^{\,j} + p_i S_i \vec{n}_i \cdot \delta\vec{A}_i^{\,j,k}\} + \sum_{i=1}^{n_n} m_i \delta\vec{A}_i^{\,j,k}\cdot\vec{g} \quad (41)$$

The still water loads are not included in the coupled-analysis because the terms related with the loads are dropped in Eq. (40). Eq. (41) should be improved in the future according to the work of Senjanović et al. (2013).

In weakly nonlinear computation, fluid restoring cannot be expressed in a form of matrix as linear restoring because pressure integration region instantaneously changes. As a result, C_R has only the gravity restoring component and fluid restoring is moved to right hand side (R.H.S) of Eq. (34). The fluid restoring on the exact body position is calculated as

$$p_{NR} = -\rho g z(t) + \rho g z(0) \quad (42)$$

The forcing vector in R.H.S. of Eq. (22) is expressed as follows:

$$(f^j)_{linear} = f_{SP}^j + f_{DAM}^j + f_{LT}^j \quad (43)$$

$$(f^j)_{nonlinear} = f_{SP}^j + f_{DAM}^j + f_{LD}^j + f_{NF}^j + f_{NR}^j + f_{SL}^j \quad (44)$$

Artificial soft spring is used to moor surge, sway, and yaw motions (Kim and Kim, 2008), which act as external force. The damping includes the damping of soft spring, viscous damping for roll motion, and structural damping of flexible motion. Those forces are calculated using linear models. The spring and damping coefficients in the linear models should be properly chosen according to the operation condition and property of the ship. The fluid forces are calculated as follows:

$$f_{LT}^j = \iint_{\bar{S}_B} p_{LT}\vec{n}\cdot\vec{A}^j\,ds \quad (45)$$

$$f_{LD}^j = \iint_{\bar{S}_B} p_{LD}\vec{n}\cdot\vec{A}^j\,ds \quad (46)$$

$$f_{NF}^j = \iint_{S_B} p_{NF}\vec{n}\cdot\vec{A}^j\,ds \quad (47)$$

$$f_{NR}^j = \iint_{\bar{S}_B} -\rho g z(t)\vec{n}\cdot\vec{A}^j\,ds + \iint_{\bar{S}_B} \rho g z(0)\vec{n}\cdot\vec{A}^j\,ds \quad (48)$$

$$f_{SL}^j = \begin{cases} \int_{S_{SL}} \frac{\partial M_a}{\partial t}\dot{h}(0,0,1)\cdot\vec{A}^j\,dx & \text{(wedge approximation)} \\ \iint_{S_{SL}} p_{GWM}\vec{n}\cdot\vec{A}^j\,dS & \text{(GWM).} \end{cases} \quad (49)$$

2.6. 2-D analysis of cross-section and structural discontinuity

A complicated geometry of cross-section makes beam modeling difficult. In order to calculate the torsional modulus, warping modulus, and shear stress flow, so-called 2-D analysis is required. An efficient method to calculate these values is finite element method. Cross-sections of ship structures are thin-walled in most cases, so they can be modeled by line elements in a plane. WISH-BSD, which is 2-D analysis code based on 2-D finite element method, has been developed as a part of WISH-FLEX JIP. The 2-D analysis method follows the works of Kawai (1973) and Fujitani (1991). This code can generate 2-D cross-sections using 1-D line elements from 3-D FE model, which means that the geometry of the element is a line and its property linearly changes along the line. Only 2-D elements such as membrane, plate and shell elements in the 3-D FE model are taken into account for the analysis. Shell element is commonly used as a property of tri or quad element. Fig. 6 shows an example of conversion from 3-D FE model to 2-D FE model. In Fig. 5, the quad elements in 3-D FE model are converted to line elements in 2-D cross-section. Beam and point mass elements are added to stiffness and inertial properties, which do not directly affect the 2-D analysis of cross-section.

Structural discontinuities due to bulkheads or deck openings are known for having a significant effect on the torsional rigidity of warping-dominant structures. Specifically, warping distortion induces bulkheads deformation, and the bulkheads resist warping. Senjanović et al. (2009b) have proposed a method to consider the effect of bulkheads on torsional rigidity. The method is based on the principle of energy under the assumption that the bulkheads only reduce the intensity of warping.

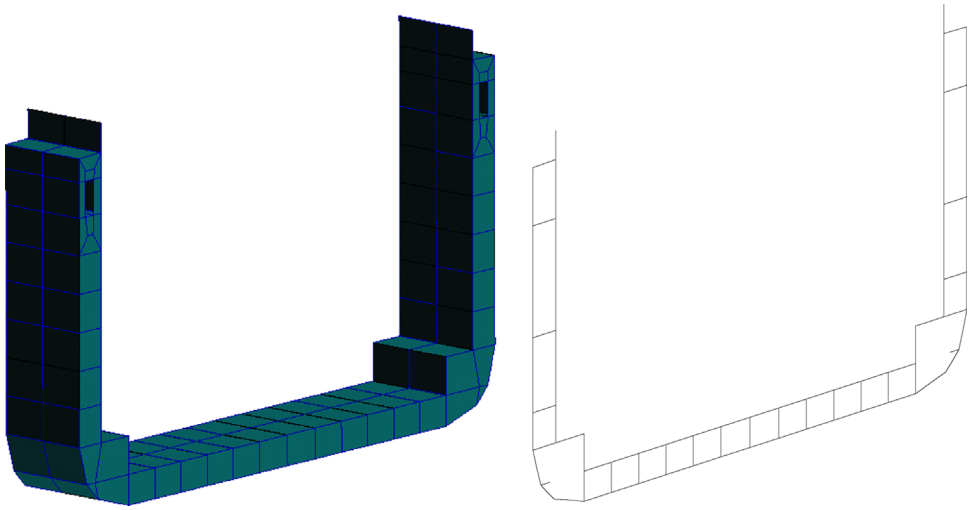

Fig. 6. 3-D FE model consists of shell elements (left) and 2-D section consists of line elements (right).

3. Numerical scheme

3.1. Spatial and temporal discretization

The domain of the boundary integral equation consists of free and body surface boundaries. The boundaries are discretized by panels, and the equation is changed to a system of algebraic equations. A bi-quadratic spline function is used to interpolate the velocity potential, the wave elevation, and the normal velocity on the panels as

$$\phi_d(\vec{x},\ t)=\sum_{j=1}^{9}(\phi_d)_j(t)B_j(\vec{x}) \tag{50}$$

$$\zeta_d(\vec{x},\ t)=\sum_{j=1}^{9}(\zeta_d)_j(t)B_j(\vec{x}) \tag{51}$$

$$\frac{\partial\phi_d}{\partial n}(\vec{x},\ t)=\sum_{j=1}^{9}\left(\frac{\partial\phi_d}{\partial n}\right)_j(t)B_j(\vec{x}) \tag{52}$$

The solution to the boundary integral equation is valid at the instant the equation is solved. For time-marching simulation, the free and body surface boundary conditions should be updated. The body boundary condition is updated by time integration of the body motion, and the free surface boundary conditions are updated by time integration of the normal velocity and the wave elevation on the free surfaces.

A mixed implicit–explicit Euler scheme is used to update the free surface boundary conditions. It has two steps, the first of which is to explicitly integrate the normal velocity on the free surface using the kinematic free surface boundary condition. It updates the wave elevation. The second step is to integrate the updated wave elevation using the dynamic free surface boundary condition. It can be called implicit because the updated wave elevation is integrated. Finally, the velocity potential on the free surface is updated. The discretization method follows the work of Kring (1994).

3.2. Implicit time integration of body motion

Implicit time integration methods are preferred in structural engineering because they are unconditionally stable with respect to time step size. This stability is requisite for direct integration because all modes are included in direct integration. In the study, Newmark-Beta method is used to integrate body motion in node-based coupling. The original equation (Newmark, 1959) can be rearranged as follows:

$$\ddot{\vec{u}}(t+\Delta t)=\frac{1}{\alpha\Delta t^2}(\vec{u}(t+\Delta t)-\vec{u}(t))-\frac{1}{\alpha\Delta t}\dot{\vec{u}}(t)-\left(\frac{1}{2\alpha}-1\right)\ddot{\vec{u}}(t) \tag{53}$$

$$\dot{\vec{u}}(t+\Delta t)=\frac{\chi}{\alpha\Delta t}(\vec{u}(t+\Delta t)-\vec{u}(t))+\left(1-\frac{\chi}{\alpha}\right)\dot{\vec{u}}(t)+\Delta t\left(1-\frac{\chi}{2\alpha}\right)\ddot{\vec{u}}(t) \tag{54}$$

where α and χ are 0.5 and 0.25, respectively. The equation of motion at the next time step is expressed as

$$M\ddot{\vec{u}}(t+\Delta t)+C\dot{\vec{u}}(t+\Delta t)+K\vec{u}(t+\Delta t)=\vec{f}(t+\Delta t) \tag{55}$$

By substituting Eqs. (53) and (54) into Eq. (55), the final form of the equation of motion is expressed as (Kim et al., 2009a, 2009b)

$$\begin{aligned}&\left(\frac{1}{\alpha\Delta t^2}M+\frac{\chi}{\alpha\Delta t}C+K\right)\vec{u}(t+\Delta t)=\vec{f}(t+\Delta t)\\&+M\left[\frac{1}{\alpha\Delta t^2}\vec{u}(t)+\frac{1}{\alpha\Delta t}\dot{\vec{u}}(t)+\left(\frac{1}{2\alpha}-1\right)\ddot{\vec{u}}(t)\right]\\&+C\left[\frac{\chi}{\alpha\Delta t}\vec{u}(t)+\left(\frac{\chi}{\alpha}-1\right)\dot{\vec{u}}(t)+\Delta t\left(\frac{\chi}{2\alpha}-1\right)\ddot{\vec{u}}(t)\right]\end{aligned} \tag{56}$$

Eq. (55) should be solved by an iterative sequence because the force term from the fluid domain is a function of velocity and displacement at the next time step. The fixed point iteration method conjunction with Aitken acceleration scheme is successfully applied to this problem (Kim et al., 2009a; Iron and Tuck, 1969). The acceleration scheme is necessary because when incompressible fluid is coupled with a moving structure, the impulsiveness of added mass induces slow convergence.

3.3. Explicit time integration of body motion

Explicit time integration methods are valid when all natural frequencies are in a narrow band. The time step size should be chosen according to the highest natural frequency in the equation of motion. Therefore, the explicit scheme is appropriate for modal superposition of few lower modes. It can be assumed that responses of higher modes are quasi-static and can be obtained without coupled analysis (Wu and Hermundstad, 2002; Wu and Moan, 2005). 4th order Adams–Bashfort–Moulton method is applied to time integration of the equation of modal motion in the study. In addition, the integration is initiated by 4th order Runge–Kutta method. The main advantage of the explicit scheme is that it does not require an iterative sequence because equation only has terms of the current time step. By extracting infinite frequency added mass from the forcing term in the fluid domain, better stability of the solution with respect to time step size can be achieved. The equation at the current time step is expressed as

$$\begin{Bmatrix}\ddot{\xi}_1(t)\\ \ddot{\xi}_2(t)\\ \vdots\\ \ddot{\xi}_{6+n}(t)\end{Bmatrix}=[M+M(\infty)]^{-1}\left[\vec{f}(t)-M(\infty)\begin{Bmatrix}\ddot{\xi}_1(t)\\ \ddot{\xi}_2(t)\\ \vdots\\ \ddot{\xi}_{6+n}(t)\end{Bmatrix}-K\begin{Bmatrix}\xi_1(t)\\ \xi_2(t)\\ \vdots\\ \xi_{6+n}(t)\end{Bmatrix}\right] \tag{57}$$

where ξ_n is the modal displacement, the subscript n is the mode number, subscripts 1–6 denote rigid motion and subscripts 7 and higher denote flexible motion, and $M(\infty)$ is the infinite frequency added mass matrix. 4th order Adams–Bashforth–Moulton method is expressed as follows:

$$\begin{aligned}\dot{\xi}'(t+\Delta t)=\dot{\xi}(t)+\frac{\Delta t}{24}[&55\ddot{\xi}(t,\ \dot{\xi}(t))-59\ddot{\xi}(t-\Delta t,\ \dot{\xi}(t-\Delta t))\\&+37\ddot{\xi}(t-2\Delta t,\ \dot{\xi}(t-2\Delta t))-9\ddot{\xi}(t-3\Delta t,\ \dot{\xi}(t-3\Delta t))]\end{aligned} \tag{58}$$

$$\begin{aligned}\dot{\xi}(t+\Delta t)=\dot{\xi}(t)+\frac{\Delta t}{24}[&9\ddot{\xi}(t+\Delta t,\ \dot{\xi}(t+\Delta t))+19\ddot{\xi}(t,\ \dot{\xi}(t))\\&-5\ddot{\xi}(t-\Delta t,\ \dot{\xi}(t-\Delta t))+\ddot{\xi}(t-2\Delta t,\ \dot{\xi}(t-2\Delta t))]\end{aligned} \tag{59}$$

Once the acceleration vector is obtained by solving Eq. (57), velocity and displacement are updated by 4th order Adams–Bashforth method in Eq. (58) as a predictor. Next, Eq. (57) is solved again to calculate the corrected acceleration vector, and the final values of velocity and displacement are recalculated by 4th order Adams–Moulton method in Eq. (59) as a corrector.

3.4. Mapping of GWM solution

Computation burden of GWM is not light even though it is a 2-D method. Slamming sections may experience water entry events with various initially submerged depths. Strictly, for each water entry event, GWM solver should be run with the corresponding initial condition. Unfortunately, it leads to slow computation in time domain analysis. In order to reduce computation burden for GWM, a mapping scheme is used between GWM solutions with different initial conditions. A solution of GWM is independent of time histories of water entry motions because a gravity term is dropped off in the dynamic free surface condition. It means that the solution only depends on the initially submerged

depth and the current water entry motion. For the mapping, the water entry problem is solved with the zero initial condition, which starts to enter the water from the zero submerged depth with a unit velocity. The solution of the problem is related to other slamming events with non-zero initial conditions.

It is simple to relate two different initial value problems by applying offsets in the pile-up of the free surface. First, the water entry problem is solved for the section from the non-submerged condition to the fully-submerged condition. The solution of the problem is the pre-processed solution. In the solution, the submerged depth is decomposed into the penetration depth due to the relative vertical motion and the free surface elevation due to the water entry. When the section starts to enter the water from the depth of A, the wave elevation of $W(A)$ can be found from the pre-processed solution. If the section penetrates the depth of C into the water, the corresponding solution should have the total submerged depth of $C+W(C)-W(A)$. The modified penetration depth of X is obtained by solving the equation of $X+W(X)=C+W(C)-W(A)$. The validity of the equation is simply confirmed by applying $A=0$ or $A=C$.

3.5. Sectional force calculation

Sectional force can be calculated directly by a beam element stiffness matrix and displacements at two end nodes in a beam theory model. In the case of 3-D FE model, integration of stress or stress times moment arm corresponds to the sectional force according to its definition. As an alternative method, sectional force can be calculated by integration of the inertial force due to flexible motions in the modal superposition method. The equation of eigenvalue analysis guarantees that the sectional force or stress can be converted to the equivalent inertial force. The procedure is as follows. First, modal accelerations equivalent to modal displacements are calculated as Eq. (60). Next, nodal accelerations are calculated using eigenvectors as Eq. (61). Finally, the sectional force is calculated by lengthwise integration of inertial forces due to the nodal accelerations as Eq. (62).

$$\begin{Bmatrix} \ddot{\xi}'^{7}(t) \\ \vdots \\ \ddot{\xi}'^{6+n}(t) \end{Bmatrix} = -M^{-1}C_S \begin{Bmatrix} \xi^{7}(t) \\ \vdots \\ \xi^{6+n}(t) \end{Bmatrix} \tag{60}$$

$$\ddot{\vec{u}}'(t) = \begin{bmatrix} \vec{A}^{7} \cdots \vec{A}^{6+n} \end{bmatrix} \begin{Bmatrix} \ddot{\xi}'^{7}(t) \\ \vdots \\ \ddot{\xi}'^{6+n}(t) \end{Bmatrix} \tag{61}$$

$$f^j_{sf}(x_p,\ t) = \int_{x_p}^{L} \vec{s}^{\,j} \cdot \hat{M} \cdot \ddot{\vec{u}}'(t)dx = \sum_{i=1}^{m} \delta_i \vec{s}^{\,j}_i \cdot \hat{M}_i \cdot \ddot{\vec{u}}'_i(t)$$
$$\delta_i = \begin{cases} 1 & \text{if } \ x_p \le x - \text{coordinate of } i\text{th node} \\ 0 & \text{otherwise} \end{cases} \tag{62}$$

For example, the coefficient vector for axial force is $\vec{s}^{\,1} = \begin{bmatrix} 1 & 0 & 0 & 0 & 0 & 0 \end{bmatrix}^T$. This method is very convenient for 3-D FE model because treating 2-D elements is complicated work. For integration of stress, corresponding elements should be distinguished and corresponding stress, area, and direction should be calculated.

In the sectional force calculation by superposition of lower mode displacements, a critical problem is that shear forces or moments far from the mid-ship section hardly converge within few lower modes. Moreover, it is not easy to obtain enough number of higher modes in eigenvalue analysis because eigenvalues of 3-D FE model are easily polluted by local modes over a particular frequency.

In contrast to modal superposition method, direct integration method always gives converged sectional force, which integrates all forces such as fluid pressure, gravity and inertial forces, and any other external forces. It is a very straightforward method to obtain converged sectional force. The sectional force by direct integration is calculated as

$$f^j_{sf}(x_p,\ t) = \begin{cases} \int_{x_p}^{L} \vec{s}^{\,j} \cdot (\vec{f}_{SP} + \vec{f}_{DAM} + \vec{f}_{LT} + \vec{f}_{LR} + \vec{f}_{IN} + \vec{f}_{G})dx & \text{(linear)} \\ \int_{x_p}^{L} \vec{s}^{\,j} \cdot (\vec{f}_{SP} + \vec{f}_{DAM} + \vec{f}_{LD} + \vec{f}_{NF} + \vec{f}_{NR} + \vec{f}_{SL} + \vec{f}_{IN} + \vec{f}_{G})dx & \text{(nonlinear)} \end{cases} \tag{63}$$

All forces can be integrated along the longitudinal axis except soft spring and damping forces because they are defined as modal force. They can be converted to equivalent acceleration as follows:

$$\begin{Bmatrix} \ddot{\xi}'^{1}(t) \\ \vdots \\ \ddot{\xi}'^{6+n}(t) \end{Bmatrix} = -M^{-1} \begin{Bmatrix} f^1_{SP} + f^1_{DAM} \\ \vdots \\ f^{6+n}_{DAM} \end{Bmatrix} \tag{64}$$

$$\ddot{\vec{u}}'(t) = [\vec{A}^{1} \cdots \vec{A}^{6+n}] \begin{Bmatrix} \ddot{\xi}'^{1}(t) \\ \vdots \\ \ddot{\xi}'^{6+n}(t) \end{Bmatrix} \tag{65}$$

In case of nonlinear computation with GWM, the sectional force is calculated as

$$\begin{aligned} f^j_{sf}(x_p,\ t) &= \int_{x_p}^{L} \vec{s}^{\,j} \cdot \hat{M} \cdot \ddot{\vec{u}}(t)dx + \iint_{x_p < x(S) < L} \vec{s}^{\,j} \cdot \vec{n}\, pdS \\ &\quad + \int_{x_p}^{L} g\vec{c}^{\,j} \cdot \hat{M} \cdot \vec{u}_g(t)dx + \int_{x_p}^{L} \vec{s}^{\,j} \cdot \hat{M} \cdot \ddot{\vec{u}}'(t)dx \\ &= \sum_{i=1}^{m} \delta_i \vec{s}^{\,j}_i \cdot \hat{M}_i \cdot \ddot{\vec{u}}_i(t) + \sum_{k=1}^{n} \delta_k \vec{s}^{\,j}_k \cdot \vec{n}\, p_k S_k + \sum_{i=1}^{m} g\delta_i \vec{c}^{\,j}_i \\ &\quad \cdot \hat{M}_i \cdot \vec{u}_g(t) + \sum_{i=1}^{m} \delta_i \vec{s}^{\,j}_i \cdot \hat{M}_i \cdot \ddot{\vec{u}}'_i(t) \end{aligned}$$
$$\delta_i = \begin{cases} 1 & \text{if } \ x_p \le x - \text{coordinate of } i\text{th node} \\ 0 & \text{otherwise} \end{cases}$$
$$\delta_k = \begin{cases} 1 & \text{if } \ x_p \le x - \text{coordinate of the center of } k\text{thpanel} \\ 0 & \text{otherwise} \end{cases} \tag{66}$$

The equivalent acceleration due to soft spring and damping is obtained by Eqs. (64) and (65). In Eq. (66), the first, second, third, and fourth integrals are the contributions of inertial, fluid, gravity, and the other forces, respectively. The second integral is decomposed into each pressure contribution because linear, nonlinear, and GWM pressures which have different grids. The effective displacement vector for gravity is expressed as

$$\vec{u}_g(t) = \vec{u}(t) - \begin{bmatrix} u^n_x(t) & u^s_y(t) & 0 & 0 & 0 & 0 \end{bmatrix}^T \tag{67}$$

The coefficient vector for gravity force is expressed as

$$\vec{c}^{\,j} = \begin{cases} \begin{bmatrix} 0 & 0 & 0 & 0 & 0 & 0 \end{bmatrix}^T & (j = 1,\ 2,\ 3,\ \text{or } 6) \\ \begin{bmatrix} 0 & 1 & 0 & 0 & 0 & 0 \end{bmatrix}^T & (j = 4) \\ \begin{bmatrix} 1 & 0 & 0 & 0 & 0 & 0 \end{bmatrix}^T & (j = 5) \end{cases} \tag{68}$$

The gravity force contributes only vertical bending and torsional moments as Eq. (68).

In direct integration, it is important to consider all forces. As a result, the final form of the sectional force becomes complicated as Eq. (66). In order to calculate converged stress, all the forces in Eq. (63) should be applied to 3-D FE model as pressure and nodal force. This static analysis of 3-D FE model will be performed in the near future.

3.6. Numerical modeling and computational parameters

A computational result highly depends on numerical modeling and parameters in time domain simulation. There are two issues, one of which is stability of simulation and the other is a convergence of result. The issues are due to spatial and temporal discretization. In this part, general characteristic of the discretization are discussed. A convergence test is important for reliable computation.

The fully-coupled hydroelastic analysis uses spatially discretized models as follows: a linear panel model for 3-D Rankine panel method, a nonlinear body panel model for weakly nonlinear approach, a set of slamming sections for GWM or wedge approximation, and 1-D/3-D FE models for FEM. In the spatial discretization, errors due to rough discretization should be minimized by a convergence test with various meshes.

The linear panel model consists of panels on the free surface and mean body surface. It is important to properly distribute panels on the free surface in the linear panel model. A convergence test should be done with various panel sizes and radiuses of the free surface. A thorough study on errors of time domain Rankine panel method were done by Kring (1994). The nonlinear panel model consists of panels on the whole body surface for calculation of nonlinear Froude–Krylov and restoring pressure on the instantaneously wetted surface.

The ship is discretized into vertical slamming sections for slamming load calculation. The number of slamming sections for the converged result should be obtained by a convergence test in waves. It should be noted that a sequential water entry of the sections always induces an error. If the frequency of the sequential entry is equal to the natural frequency, the error is drastically increased by the resonance.

A convergence test for 1-D/3-D FE model for the coupled-analysis can be done by eigenvalue analysis. If 10 flexible modes are included in the coupled-analysis, eigenvalues of the 10 modes should be the converged values. It should be noted that 3-D FE model for stress assessment requires finer mesh than that for motion and sectional force calculation in the coupled analysis.

The next step is to determine the number of flexible modes for the converged solution of the coupled-analysis. It can be obtained by a convergence test in waves. It only guarantees the assumption in 3-D FE model part, that responses of higher modes excluded in the coupled analysis are quasi-static and vanishingly small in the fluid–structure interaction. It should be noted that the number of flexible modes for converged stress or sectional force by modal superposition is much larger than that for the coupled-analysis. It is more reliable to calculate converged stress by an additional FE analysis with the coupled-analysis result compared to the modal superposition.

The main numerical parameter is the time step size in time domain simulation. In the coupled-analysis, there are two parts of time integration, which are the free surface condition and the equation of motion. GWM is not directly related with the time step size because the temporal integration is replaced with the spatial integration (Khabakhpasheva et al., 2014). The time step size should be chosen by a convergence test. If the time step size is too large, an error due to the temporal discretization can induce a numerical damping in implicit integration schemes or an instability in explicit integration schemes.

In the coupled-analysis, it is very hard to predict to errors due to the temporal and spatial discretization because the errors are aggravated by coupling schemes and spread to other domains. Thus, it is needed to conduct convergence tests for each wave and operation condition. User's experience may help to reduce a burden of the tests. It should be noted that all the results shown in Section 4 are obtained through convergence tests. In this paper the details about the convergence tests are skipped.

4. Analysis results

4.1. 60 m barge

The 60 m barge model is chosen as the first test case for two purposes. One is to indirectly validate numerical models by a

Table 1
Principle dimensions of the 60 m barge.

Type	Value
Length (m)	60.0
Breadth (m)	10.0
Height (m)	4.0
Hull thickness (m)	0.001
Young's modulus (GPa)	200.0
Hull density (ton/m^3)	714.3
Bulkhead thickness (m)	1.0
Bulkhead spacing (m)	0.5
Total weight (ton)	1200.0

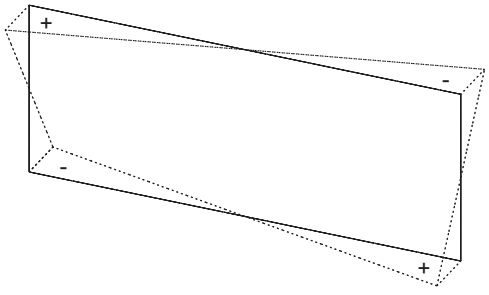

Fig. 8. Warping distortion of the 60 m barge w/o B.H.

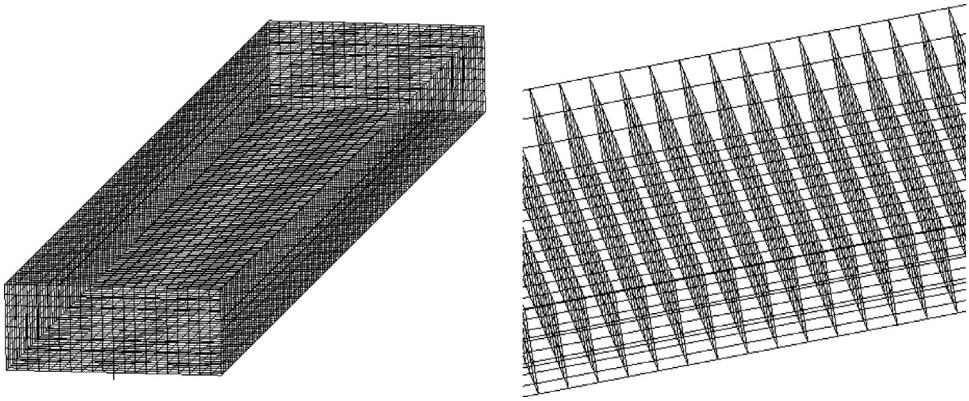

Fig. 7. 3-D FE model of the 60 m barge: outer shape (left) and inner structure (right).

comparison with each other because the beam theory model, WISH-FLEX BEAM, were validated against the experiment for the flexible barge in Ecole Centrale de Marseille (Kim et al., 2009a, 2009b, 2009c). In addition, the fluid part, WISH, were validated against the experiment of S175 (Kim and Kim, 2008). The other purpose is to compare results with minimized difference between the numerical models in modeling.

The principle dimensions are shown in Table 1. It is composed of 16,000 shell elements. The barge can be thought of as globally soft and locally stiff like a beam. This characteristic is achieved by very stiff bulkheads in the longitudinal direction. Fig. 7 shows the outer shape and the bulkheads. The bulkheads are modeled as zero mass. The 1st to 20th modes are obtained by eigenvalue analysis without local modes, and the 7th to 20th flexible modes are compared. Commercial software NASTRAN is used to perform the eigenvalue analysis.

The bulkheads completely constrain the in-plane deformation of the cross-section. This leads to changes in the stress–strain relationship of shell elements on the hull. The original relationship is expressed as

$$\begin{Bmatrix}\sigma_x\\ \sigma_y\\ \tau_{xy}\end{Bmatrix}=\frac{E}{1-\nu^2}\begin{bmatrix}1 & \nu & 0\\ \nu & 1 & 0\\ 0 & 0 & (1-\nu)/2\end{bmatrix}\begin{Bmatrix}\varepsilon_x\\ \varepsilon_y\\ \gamma_{xy}\end{Bmatrix} \tag{69}$$

Let us consider an element exposed to tensile loading in the x-direction. If there is no constraint, the y-direction strain is induced, the amount of which makes the normal stress zero in the y-direction. On the other hand, if the bulkheads of the model completely suppress the strain in the y-direction, an additional normal stress in the x-direction is induced. It is derived by substituting Eq. (69) into Eq. (70).

$$\varepsilon_y=\begin{cases}-\nu\varepsilon_x & w/o\ \text{bulkhead}\\ 0 & \text{with bulkhead}\end{cases} \tag{70}$$

By integrating the normal stress in the x-direction over the distance from the neutral axis on the cross-section, so-called bending rigidity is obtained as in Eq. (71). The bending rigidity is increased by $1/1-\nu^2(=1.09)$ times when the Poisson ratio is 0.3. Axial rigidity is also calculated in the same manner and the same coefficient is derived.

$$M=\left(\frac{1}{1-\nu^2}\right)EI\frac{\partial\theta}{\partial x} \tag{71}$$

Warping distortion of the cross-section is shown in Fig. 8. The bulkheads completely suppress the distortion, and the Saint-Venant torsional modulus becomes equal to the polar moment of inertia. Consequently, the torsional modulus is increased by the bulkheads.

Timoshenko beam theory assumes constant shear stress along the cross-section contour and requires calculation of the effective shear factor. These are calculated based on the classical energy approach as

$$K_y=\frac{1}{A\int\tau_{sy}{}^2tds} \tag{72}$$

The shear stress is obtained by the 2-D analysis of the cross-section. The flows of shear stress of the cross-section with and without bulkheads are shown in Fig. 9. The shear stress is constant on the side walls and zero on the top and bottom walls because the bulkheads are very stiff. The stiffness properties with and without the bulkheads are compared in Table 2. All the rigidities are increased by the bulkhead except warping, and the increments are not negligible.

Natural frequencies and mode shapes in dry mode are compared. Table 3 shows that the bulkheads play a role in the torsional rigidity and the assumption about the bulkheads is adequate. Slight differences are found in the higher modes but will vanish if the number of beam elements increases. In this case, the beam model consists of 31 uniform beam elements.

Eigenvectors of the 3-D FE model are recalculated at nodes of the beam model and compared to each other. Fig. 10 shows the eigenvectors at the reference axis on the mass center. Here, capital T and R mean translational and rotational displacements, respectively, and subscripts denote the directions of the displacements. The displacements are generalized to make diagonal components

Table 2
Cross-section properties of the 60 m barge.

Type	w/o B.H.	With B.H.
A (m^2)	0.028	0.031
Iy (m^4)	0.091	0.099
Iz (m^4)	0.367	0.403
Ky	0.661	0.714
Kz	0.171	0.285
J (m^4)	0.228	0.280
Iw (m^6)	0.037	0.000

Table 3
Natural frequencies of the 60 m barge in dry mode (Hz).

Mode no.	Beam w/o B.H.	Beam with B.H.	3-D FE model
7 (2-V.B.)	0.85	0.92	0.92
8 (2-H.B.)	1.63	1.72	1.72
9 (2-Tor.)	1.93	2.13	2.13
10 (3-V.B.)	1.98	2.23	2.23
11 (4-V.B.)	3.25	3.77	3.77
12 (3-H.B.)	3.70	3.89	3.89
13 (3-Tor.)	3.87	4.26	4.27
14 (2-Axial)	4.39	4.62	4.62
15 (5-V.B.)	4.52	5.39	5.37
16 (4-H.B.)	6.03	6.31	6.31
17 (4-Tor.)	5.86	6.39	6.40
18 (6-V.B.)	5.78	7.01	6.98
19 (5-Tor.)	7.92	8.53	8.53
20 (7-V.B.)	7.02	8.62	8.57

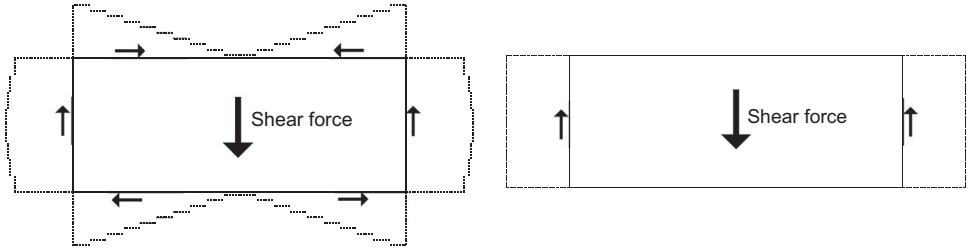

Fig. 9. Shear stress flows of the 60 m barge w/o B.H. (left) and with B.H. (right).

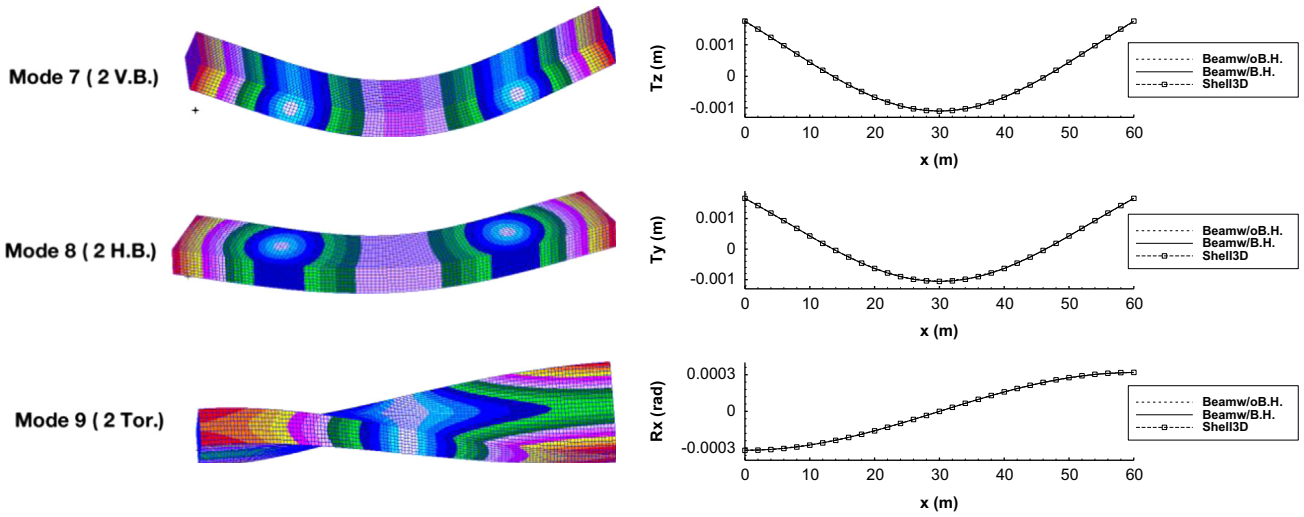

Fig. 10. Eigenvectors of the 60 m barge: the 3-D FE model (left) and the beam models (right).

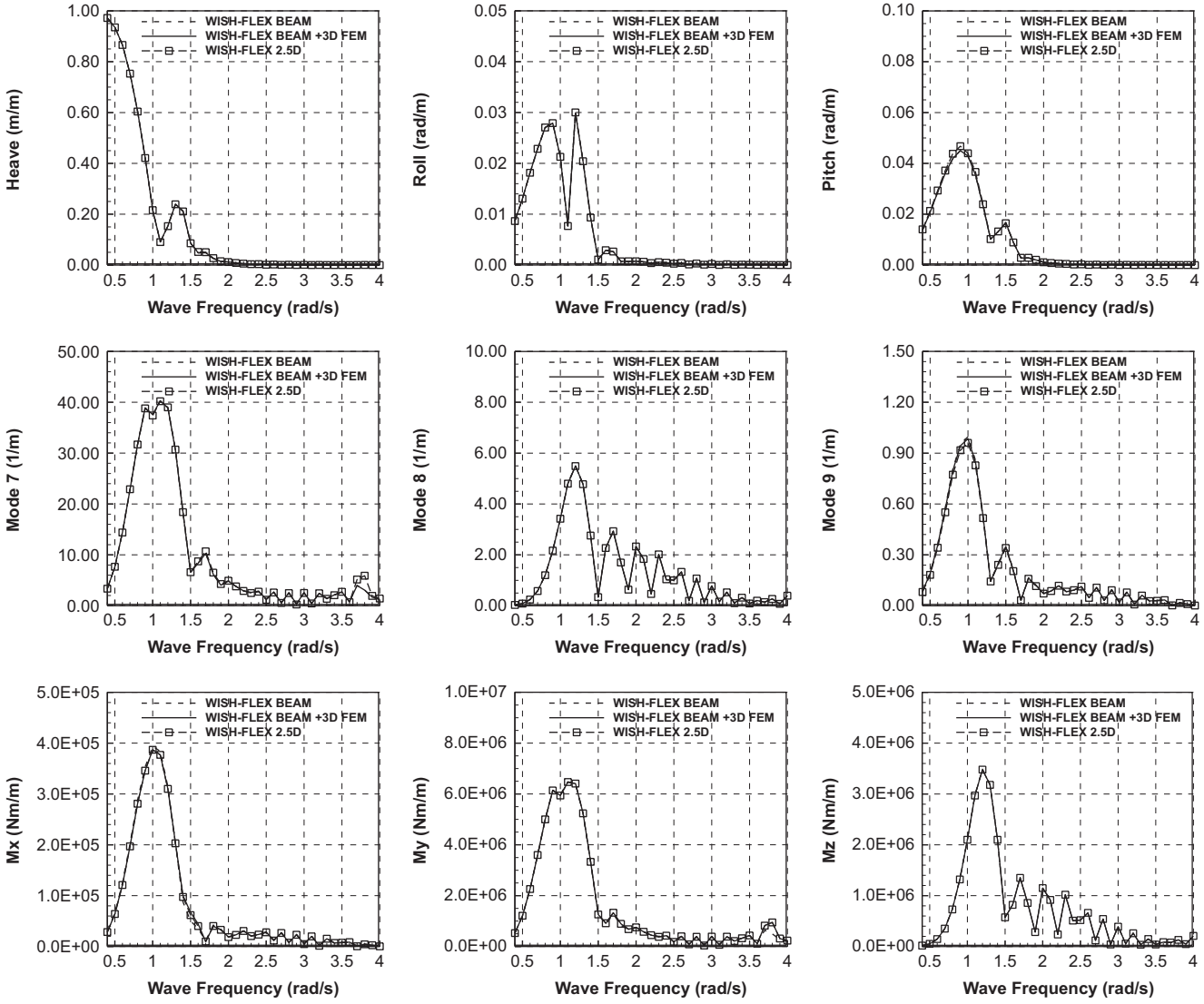

Fig. 11. RAOs of rigid body motions at the mass center, flexible motions, and sectional forces at the mid-ship section in oblique seas (linear, zero forward speed, 150° heading angle).

of modal mass matrix one. All the models show good agreement in the mode shapes. The modified beam model uses the interpolated eigenvectors of the 3-D FE model in motion analysis.

Linear computations are performed on the three structural models coupled with the 3-D Rankine panel method. In Fig. 11, all responses are shown to be almost identical. The sharp peak of roll motion is observed near the frequency of 1.2 rad/s, which corresponds to the natural frequency of roll motion. The smooth peak of roll motion is due to the relationship between the wave and ship length. A small difference between the models is found in

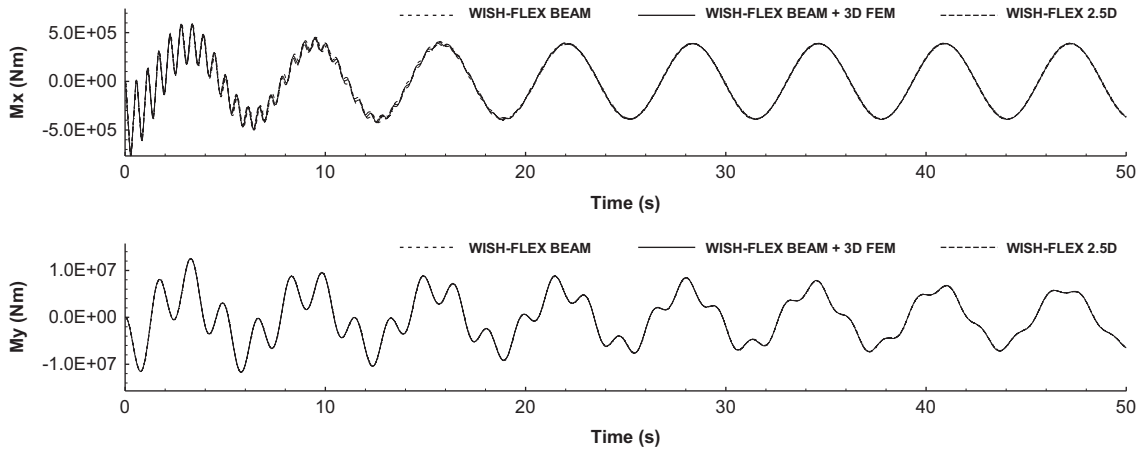

Fig. 12. Time series of sectional forces at the mid-ship section in oblique sea (linear, $H=1$ m, $T=6.3$ s, zero forward speed, 150° heading angle).

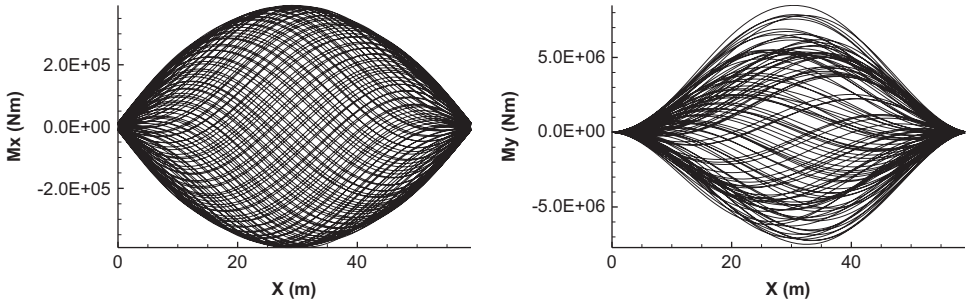

Fig. 13. Sectional load distribution along the ship length (WISH-FLEX BEAM, time >30 s, linear, $H=1$ m, $T=6.3$ s, zero forward speed, 150° heading angle).

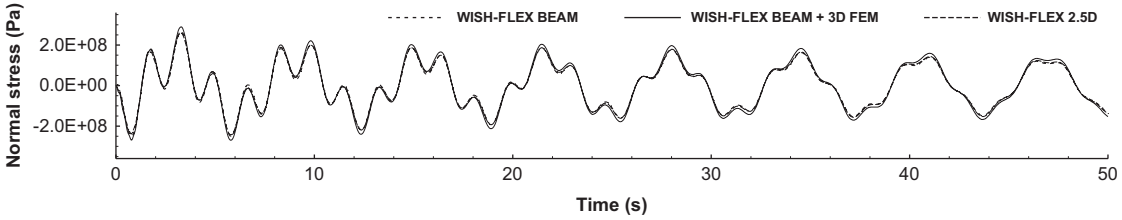

Fig. 14. Normal stress in the longitudinal direction on the top at the mid-ship section (linear, $H=1$ m, $T=6.3$ s, zero forward speed, 150° heading angle).

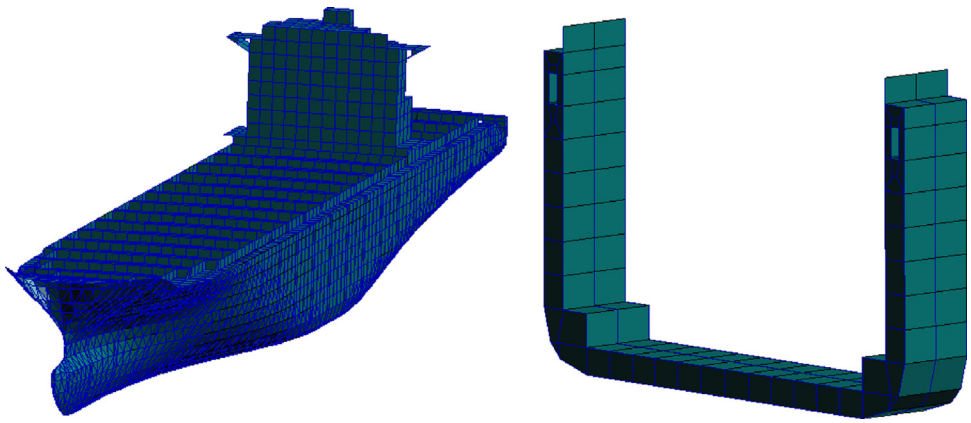

Fig. 15. 3-D FE model of the 6500 TEU containership: outer shape (left) and mid-ship part (right).

the resonant response of the 7th mode near 3.7 rad/s. The difference is acceptable because a resonant response is very sensitive to frequency. Resonant responses to linear and nonlinear wave excitations are compared in the following sections concerning the 6500 TEU and 10,000 TEU containerships.

In Fig. 12, the time series of sectional forces in the regular wave are compared. The still water loads are not included. The high-frequency oscillations in the front part of the torsional moment and vertical bending moment are transient motions of 2-node vertical bending and 2-node torsion modes. Good agreement is obtained for both wet mode natural frequencies and responses to waves. The natural frequency of 2-node vertical bending decreases from 0.92 Hz in dry mode to 0.61 Hz in wet mode. The added mass can be calculated from the wet mode natural frequency. Fig. 13 shows the longitudinal distribution of the sectional forces. It is confirmed that the system is balanced in each time step.

Fig. 14 shows the time series of normal stresses in the longitudinal direction. The stress is evaluated on the top at the mid-ship section, the coordinates of which are 30.0 m from AP, 0.0 m from the center line, 2.0 m from the water line. The stress including both quasi-static and dynamic contribution is calculated as follows:

$$\sigma_x = \frac{M_y}{I_y} z + \frac{F_z}{A} \tag{73}$$

Table 4
Principle dimensions of the 6500 TEU containership.

Type	Value
LBP (m)	286.3
Breadth (m)	40.3
Height (m)	24.1
Draft (m)	13.0
Total weight (ton)	95,276.0

$$\sigma_x = \sum_{j=7}^{k} \sigma_x^j \xi^j \tag{74}$$

where the normal stress of jth mode obtained by eigenvalue analysis of the 3-D FE model. Eq. (73) is used in the beam theory model, and Eq. (74) is used in the modified beam and 3-D FE models. The results show good agreement between the stresses of the different models. In Eq. (74), the stress converges when $k=14$. If stress is evaluated at the location far from the mid-ship, k must be larger than 14. In order to obtain the converged stress at every location, quasi-static stresses of higher modes should be calculated, which are not included in the coupled-analysis. The most rigorous method is to perform FE analysis with applying all the inertial and external forces. In addition, the mesh of the 3-D FE model should be finer than that for eigenvalue analysis. The stress evaluation is not discussed more than the above because it is too complicated to be fully handled in this study. However, the method for stress evaluation will be thoroughly discussed in the near future because stress evaluation is the final goal of the hydroelastic analysis.

Table 5
Bulkhead strain energy coefficients of the 6500 TEU containership (m^5).

	H.B.	V.B.	Contraction	Tor.
Support B.H.	19.699	0.236	0.154	1.319
Watertight B.H.	40.638	0.987	0.407	5.117

Table 6
Stool strain energy coefficients of the 6500 TEU containership (m^5).

	H.B.	Shear	Tor.
Stool	33.854	1.492	2.603

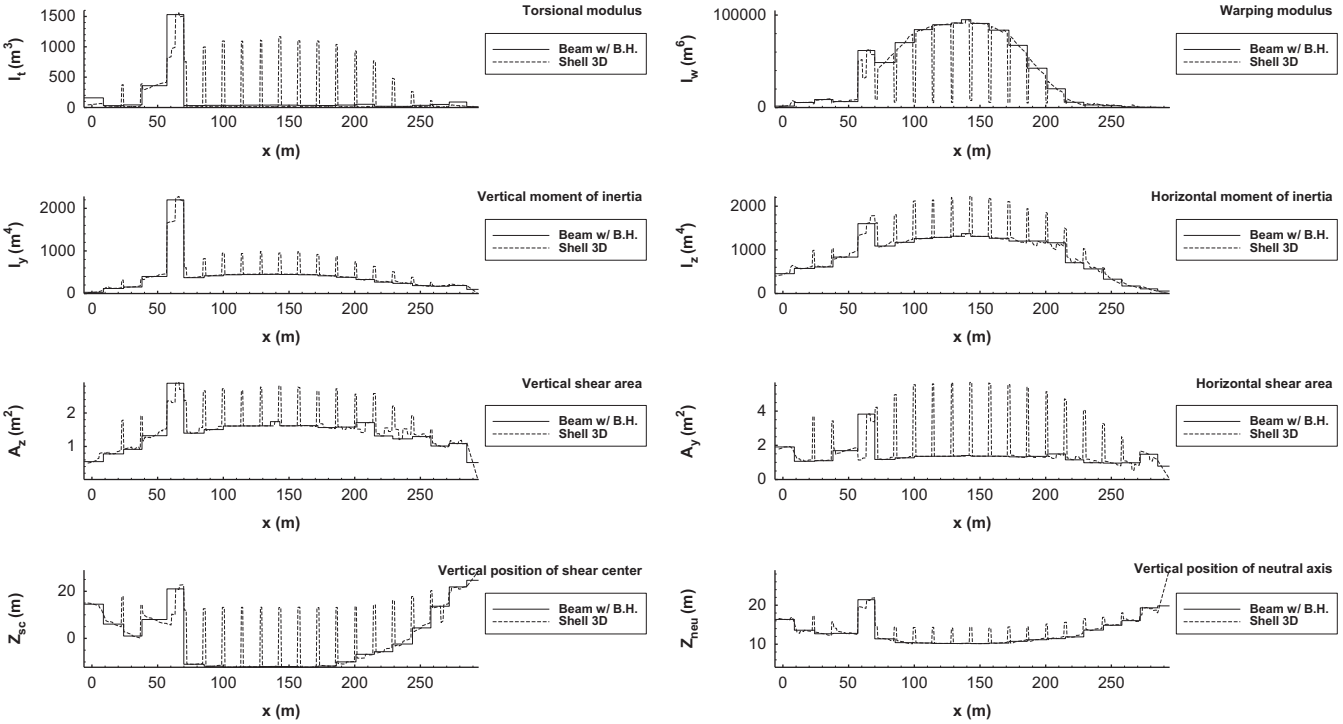

Fig. 16. Cross-section properties of the 6500 TEU containership.

4.2. 6500 TEU real containership

The second test case is the 6500 TEU containership shown in Fig. 15. The principle dimensions are shown in Table 4. Numerical simulations are conducted on the three models. The 3-D FE model is made of beam, shell, and point mass elements. It has 14,000 nodes and 40,000 elements. In order to model full-loading conditions, the container mass is modeled by point mass elements and distributed on bulkheads and hulls.

In beam modeling, a thin-walled open cross-section and bulkheads necessitate the use of 2-D analysis of the cross-section. The sectional property distribution of the 3-D FE model is calculated by WISH-BSD and plotted in Fig. 16. The accommodation deck and bulkheads induce drastic changes in the sectional properties. Sectional properties are reflected in beam modeling as the solid lines in Fig. 16. The effect of bulkheads is considered by increasing the torsional modulus according to the method by Senjanović et al. (2009b).

$$I_t^* = \left(1+\frac{a}{l_1}+\frac{4(1+\upsilon)C}{I_t l_0}\right) I_t \tag{75}$$

Eq. (75) was derived by Senjanović et al. (2009b). In Eq. (75), the second and third terms are the total bulkhead contribution to hull torsional modulus. The energy coefficients of bulkheads and stools due to warping distortion are calculated using Eqs. (59)–(62) in the paper of Senjanović et al. (2009b). Tables 5 and 6 show the energy coefficients of bulkhead and stool due to warping.

The bulkheads of the shell 3-D model are modified to be stiffer than the original design because the container mass attached to the bulkheads can cause local modes in lower frequency. Consequently, the strain energy becomes larger than that of the original design. Finally, the effect of the bulkheads is considered by increasing the torsional modulus as

$$I_t^* = (1+0.143+2.160) I_t = 3.303 I_t \tag{76}$$

The effective shear factor is calculated by integrating the shear stress flow. The shear stress flows evaluated by 2-D analysis are shown as dotted lines in Fig. 17. The distances from the dotted lines to the solid lines show the magnitudes of the shear stresses.

Dry mode natural frequencies of the beam models with and without bulkheads and the 3-D FE model are compared. Fig. 18 shows the eigenvectors of the models. The eigenvectors of the beam models are evaluated at the reference axis on the mass center. Table 7 shows the dry mode natural frequencies of the models. Good agreement is obtained in the results of 2-node torsion and 2-node vertical bending. The consideration of the bulkhead plays a role in 2-node torsion. However, the 2-node horizontal bending result shows a difference in the natural frequency and the eigenvectors.

Linear simulations are conducted on the three models. Fig. 19 compares RAOs of the models. Heave, roll, and pitch motions at

Table 7
Natural frequencies of the 6500 TEU containership in dry mode (Hz).

Mode no.	Beam w/o B.H.	Beam with B.H.	3-D FE model
7 (2-Tor.)	0.35	0.49	0.48
8 (2-H.B.)	0.64	0.72	0.75
9 (2-V.B.)	0.80	0.80	0.80
10 (3-H.B.)	1.19	1.35	1.32
11 (3-V.B.)	1.79	1.79	1.64
12 (4-H.B.)	1.70	1.87	1.75

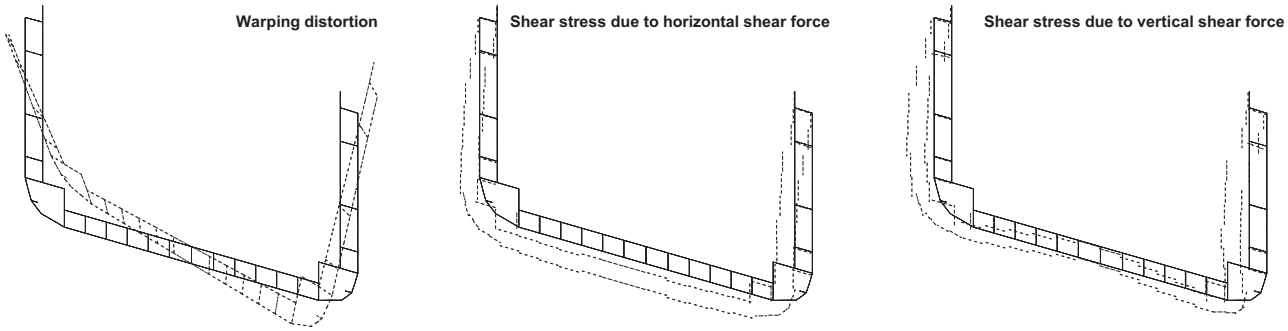

Fig. 17. 2D analysis results of the 6500 TEU containership at the mid-ship section.

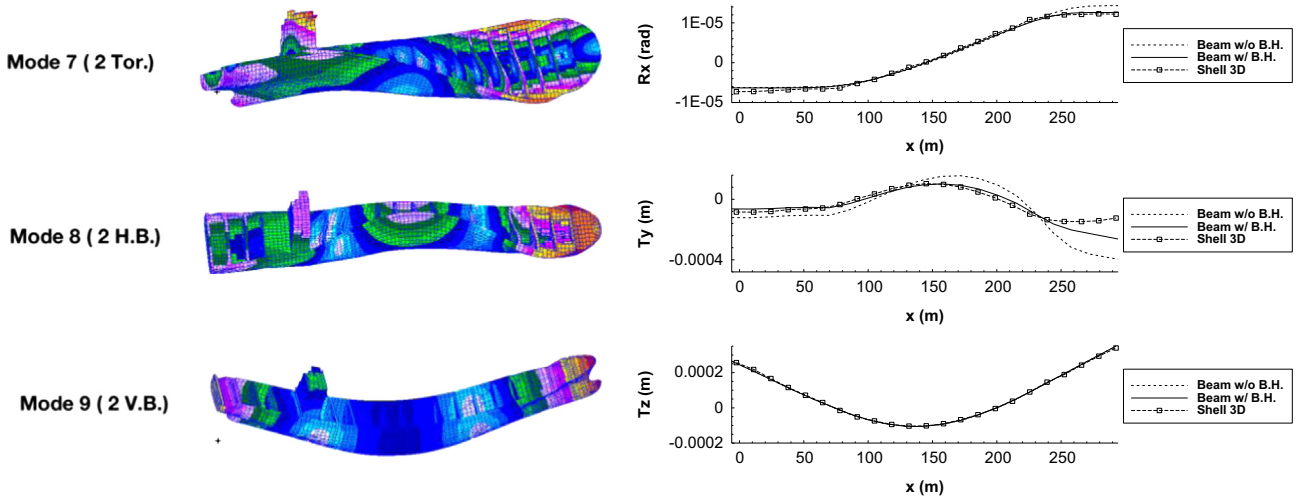

Fig. 18. Eigenvectors of the 6500 TEU containership: shell model (left) and beam models (right).

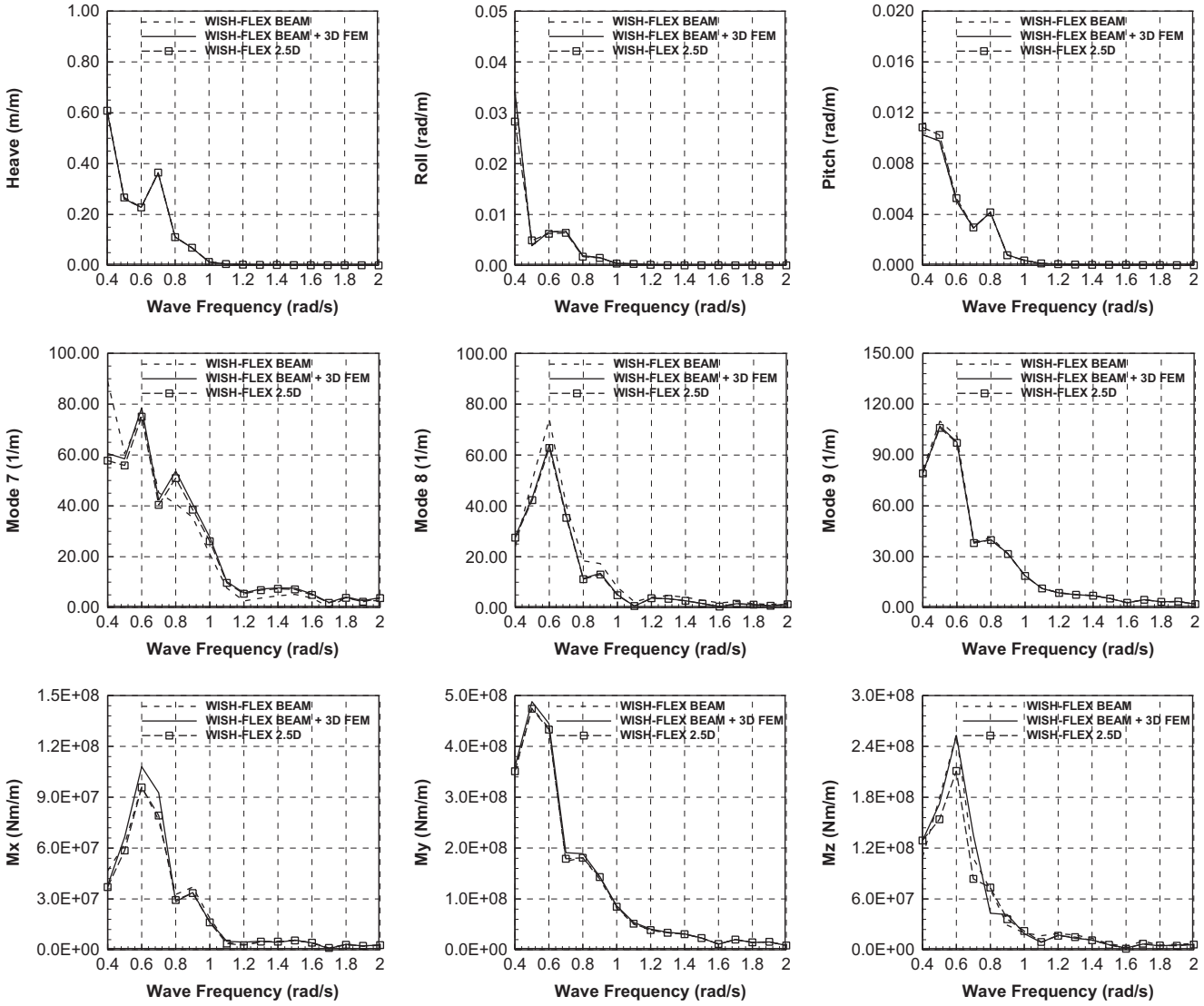

Fig. 19. RAOs of rigid body motions at the mass center, flexible motions, and sectional forces at the mid-ship section in oblique seas (linear, zero forward speed, 150° heading angle).

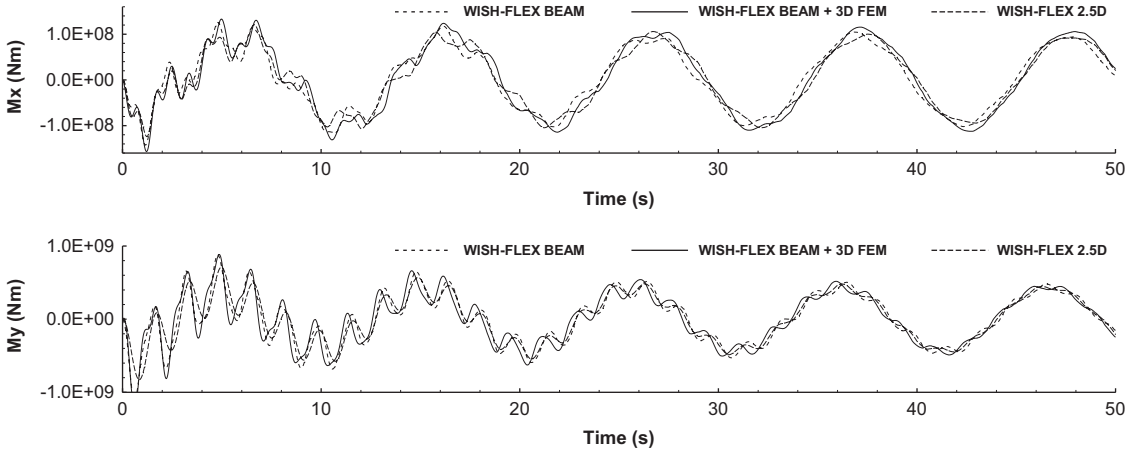

Fig. 20. Time series of sectional forces at the mid-ship section in oblique sea (linear, $H=1$ m, $T=6.3$ s, zero forward speed, 150° heading angle).

the center of mass are almost the same in all the models, which include only rigid motions. Flexible motions can be compared in modal motions or sectional forces. Small differences between the models are found in flexible motions and sectional forces. The differences are mainly due to different eigenvectors and natural frequencies. The tendency of the differences is interesting. The modified beam model shows more similar flexible motions with those of the 3-D FE model compared to those of the beam

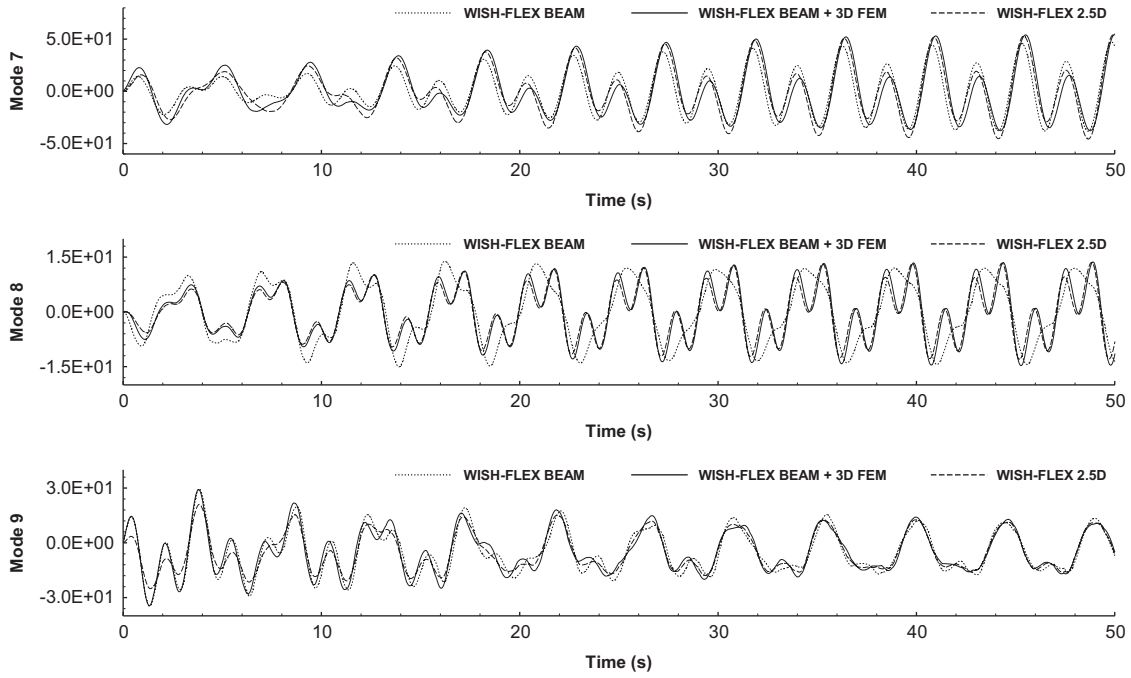

Fig. 21. Time series of modal motions in oblique sea (weakly nonlinear, $H=3$ m, $T=4.52$ s, zero forward speed, 150° heading angle).

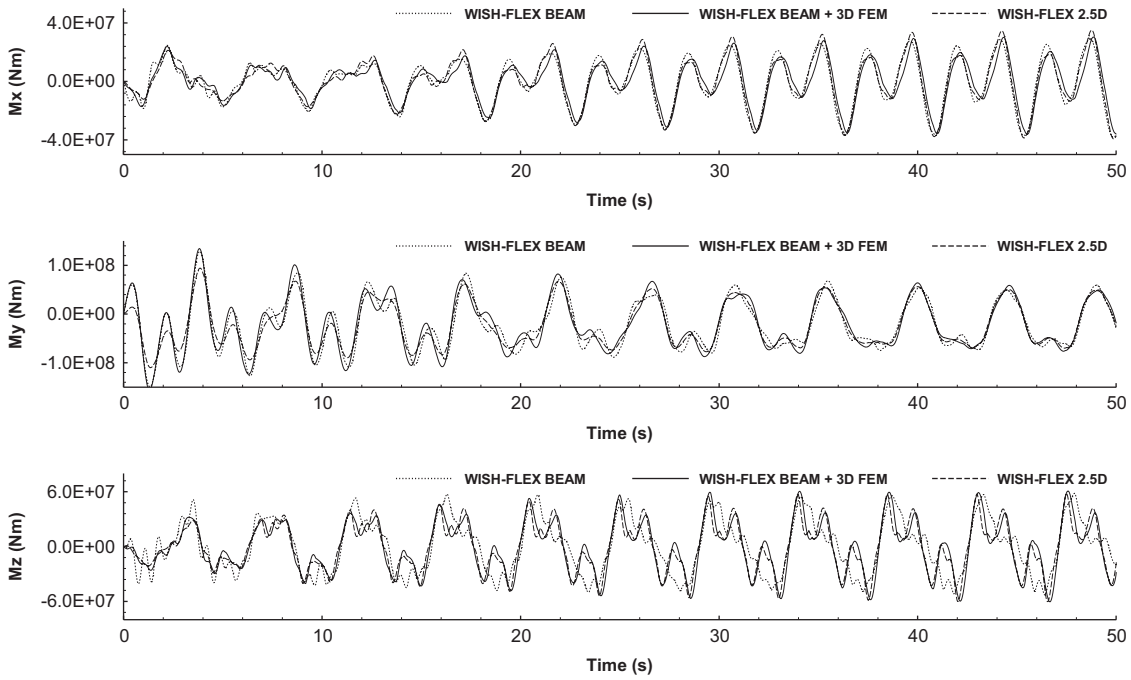

Fig. 22. Time series of sectional forces at the mid-ship section in oblique sea (weakly nonlinear, $H=3$ m, $T=4.52$ s, zero forward speed, 150° heading angle).

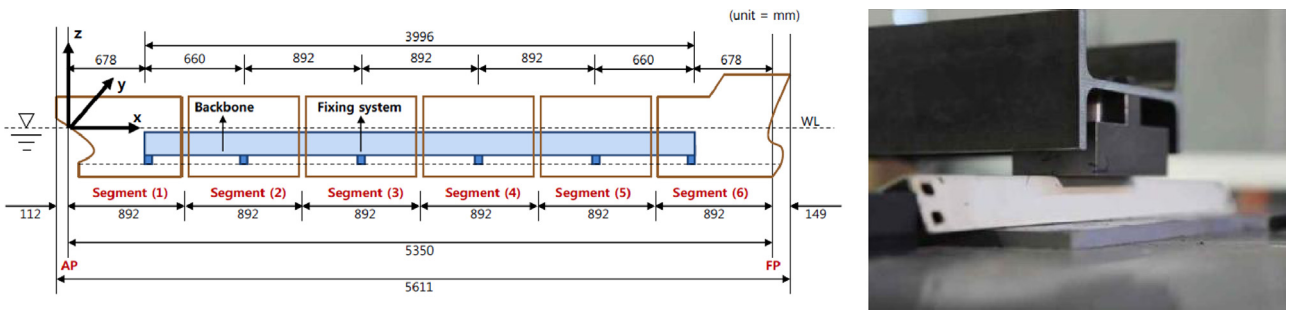

Fig. 23. Experimental model of the 10,000 TEU containership (left: configuration, right: H-shape backbone).

theory model. In the sectional forces, however, the modified beam gives a slightly overestimated result, whereas the beam theory model shows better agreement with the 3-D FE model. In Fig. 20, the modified model shows the time lag in vertical bending moment. These differences may be due to the inconsistency of the eigenvectors and mass model.

Figs. 21 and 22 show the results of nonlinear simulations based on the weakly nonlinear approach. The still water loads are not included. The wave frequency and forward speed condition are chosen for 2nd harmonic springing of 2-node torsion. The 1st and 2nd harmonic components in the 7th mode response show good agreement between the three models. The 8th mode natural frequency of the 3-D FE model is also equal to 3 times the encounter frequency. The 3rd harmonic component is clearly shown in the results of the modified beam and 3-D FE models, whereas it is small in the response of the beam theory model.

4.3. Experimental model of 10,000 TEU containership

A model test of a virtual 10,000 TEU containership has been carried out by MOERI/KORDI (2010) to investigate springing and whipping phenomena. Fig. 23 shows the experimental model, and Table 8 shows its principle dimensions. The model consists of six segmented hulls, which are connected by an H-shaped backbone. The model is connected with the towing system by 4 wires, two of which are attached to the AP and the other two are attached to the FP. The measured natural periods of surge, sway and roll motions are 87.29 s, 104.95 s, and 27.42 s in real scale, respectively. Yaw motion is also constrained by the wires, but its natural period is not measured.

The segmented body of the experimental model is directly modeled using shell elements in the 3-D FE model. In contrast, a continuous body is assumed in the beam theory model. It makes a difference of the inertial properties between the segmented body and the continuous body. The former corresponds to lumped mass, whereas the latter corresponds to consistent mass. The difference of the inertial properties vanishes if the number of nodes is sufficiently large. In this case, however, the difference will not vanish even in the lowest mode because the experimental model has only six lumped masses.

Eigenvalue analysis results are shown in Fig. 24 and Table 9. The lowest flexible mode is 2-node torsion. The difference due to the mass modeling is found in the eigenvectors as expected. The segmented body strongly affects the eigenvectors of torsional mode, which manifest in the form of discontinuous displacement. Moreover, local modes due to lumped mass are found in the result of the 3-D FE model. The local modes are the 13th and 15th modes in Fig. 25. The 2-node horizontal mode is found in the higher modes as shown in Fig. 25, but it is not taken into account in motion analysis.

For the calculation of fluid pressure, linear and nonlinear panel models and a set of slamming sections are prepared. In the linear panel model for 3-D Rankine panel method, 500 panels and 3000 panels are distributed on the mean body and free surface. 4000 panels are distributed on the whole body surface in the nonlinear panel model for weakly nonlinear approach. The ship is sliced into 40 slamming sections in the longitudinal direction for evaluation of slamming loads. The sections are perpendicular to the free surface of the calm water.

The wet mode natural frequencies of the numerical models are obtained through a hammering test, which is shown in Table 10. The hammering test is conducted by applying an impulsive load in the coupled-analysis without waves, which is same with that in the model test. A difference of about 10% between the numerical models and the experimental model is observed in the natural frequencies of 2-node torsion and 2-node vertical bending. It is not clear what causes the difference because the experimental data is insufficient. In order to simulate springing in the same frequency

Table 8
Principle dimensions of the 10,000 TEU containership.

Item	Prototype	Model
Scale	1:1	1:60
LBP (m)	336.6	5.611
Breadth (m)	48.4	0.807
Height (m)	27.2	0.453
Draft (m)	15.0	0.250
Total weight (kg)	143,741,920.0	665.472

Table 9
Natural frequencies of the 10,000 TEU containership in dry mode (Hz).

Mode no.	Beam	Mode no.	3-D FE model
7 (2-Tor.)	0.27	7 (2-Tor.)	0.26
8 (3-Tor.)	0.43	8 (3-Tor.)	0.43
9 (2-V.B.)	0.66	9 (2-V.B.)	0.63
10 (4-Tor.)	0.72	10 (4-Tor.)	0.72
11 (5-Tor.)	1.05	11 (5-Tor.)	1.05
12 (6-Tor.)	1.49	12 (3-V.B.)	1.15
13 (3-V.B.)	1.65	13 (6-Tor.)	1.26
14 (7-Tor.)	1.99	14 (4-V.B.)	1.40

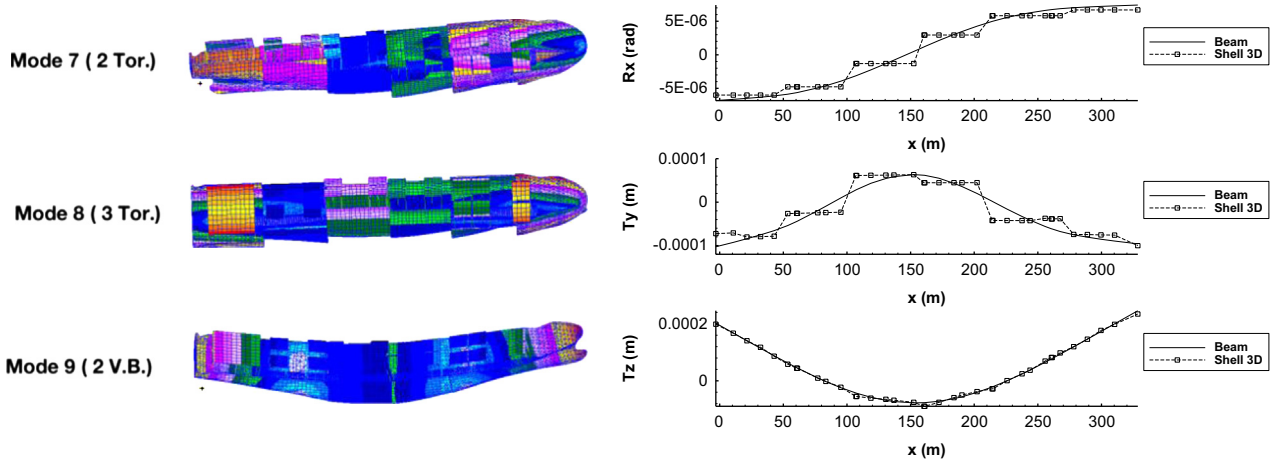

Fig. 24. Eigenvectors of the 10,000 TEU containership: 3-D FE model (left) and beam models (right).

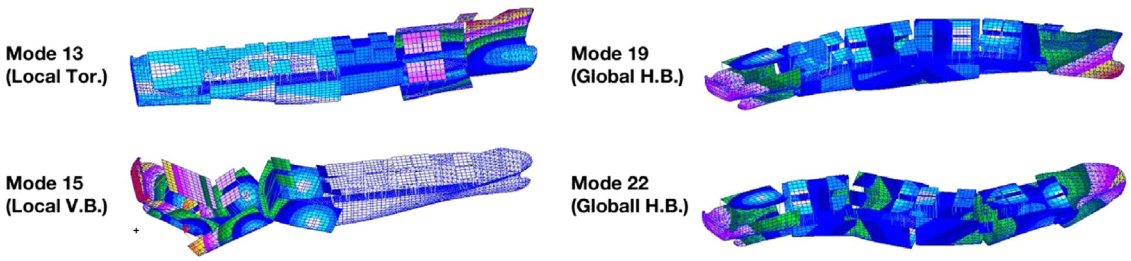

Fig. 25. Local modes in lower frequency (left) and global modes in higher frequency (right).

Table 10
Natural frequencies of the 10,000 TEU containership in wet mode (Hz).

Mode no.	Frequency	Damping ratio (%)
7 (2-Tor.)	0.30	5
9 (2-V.B.)	0.43	2

conditions as the model test, the rigidity of the backbone is adjusted according to the experimental result. The wires in the experiment are modeled by the soft spring in order to prevent drift motions. The natural periods of surge, sway, and yaw motions are about 30 s in the numerical models. The soft spring is stiffer than the wires but its effect is negligible because its frequency is much lower than the encounter frequency. It is also confirmed by tests with various stiffness of soft springs in the computation. It should be noted that all the numerical inputs and parameters are determined by the convergence and hammering tests.

Structural damping ratios of the numerical models are deduced from the total damping ratios of the experimental model since they cannot be measured directly. In the modal superposition method, damping ratios of all modes are separately handled using modal damping ratio. However, in direct integration, it is hard to model structural damping based on nodal velocity. Rayleigh damping is often used for modeling of structural damping. It can handle damping ratios of two natural modes directly but inevitably induces unwanted damping on rigid body motions because the damping matrix includes a nodal mass matrix which is not formulated in generalized coordinate system. By excluding the portion of the mass matrix from the Rayleigh damping matrix, the unwanted damping can be removed, but the number of controllable modes decreases to one.

Linear simulations in oblique seas are performed on the three models, and the results are compared with the experiment. Linear motions including both rigid and flexible motions at the center of mass are compared with the experimental data in Fig. 26. Good agreement between the numerical models and the experimental model is obtained in the motions. In addition, torsional moments at 0.33, 0.5, and 0.66 L are compared in Fig. 27.

The difference in torsional moment at the resonance frequency, 0.95 rad/s, is acceptable. However, a large discrepancy between the models is found in the vertical bending moment near the resonance frequency, 1.25 rad/s. It is difficult to determine what causes this difference because plots near the frequency are not enough in the experimental result. A possible reason is that the linear springing is not accurately produced in the experiment because it is hard to keep the regularity in the experimental condition of the high wave frequency. More elaborate experiment for linear springing should be done for a meaningful comparison. The same discrepancy between the other computation and the experiment was shown in the work of Bigot et al. (2011).

The three numerical models give similar results, but the modified beam model gives overestimated sectional forces. This is due to the inconsistency of the eigenvectors and mass model as shown in the results for the 6500 TEU containership.

In real operating conditions, the ship goes through irregular waves. Springing responses will be induced by both linear and nonlinear excitations, the frequency of which is equal to the natural frequency. One of the main excitations will be the 2nd or 3rd order component in the Froude–Krylov and restoring force, because energy densities of these frequency waves are high in most cases. Conditions for 2nd and 3rd harmonic springing simulations are shown in Table 11.

The still water loads are calculated and shown in Fig. 28 prior to a comparison of dynamic loads. Fig. 29 shows nonlinear springing responses in the above conditions. A significant difference between the numerical models and the experimental model is found in the 2nd harmonic springing of 2-node torsion. The experimental model shows larger 1st and 2nd order components than those of all the numerical models. In the 3rd harmonic springing responses of 2-node torsion, this tendency more dominantly appears. The ship has large pitch and roll motions at this frequency, so the weakly nonlinear approach may be not enough to approximate nonlinear excitation. In the case of 2-node vertical bending springing, the numerical models show larger 2nd harmonic responses compared to the experiment. However, the 3rd harmonic response is larger in the experimental model. It is considered that the tendency of the differences is related to large motions. When the ship has large rigid body motions, the springing responses tend to be smaller in the numerical simulation compared to those in the experiment.

Whipping responses to regular waves are simulated in a head sea with different forward speeds. The wave amplitude and height are 14.3 s and 6.0 m, respectively. Fig. 30 shows whipping responses to slamming loads calculated by GWM. Good agreement is observed between the numerical and experimental models in cases of 5 knots and 13.5 knots forward speeds. In case of 20.3 knots forward speed, the numerical models show larger whipping responses than those of the experimental model. In the experiment, green water occurs after bow flare slamming and it delays and reduces the second peak at 77 s in Figs. 30 and 31. Fig. 31 shows whipping responses to slamming loads calculated by wedge approximation. The results are similar with those of GWM, but wedge approximation shows slightly better agreement with the experiment. It might be due to the fact that 2-D slamming models tend to overestimate loads, but wedge approximation tends to underestimate slamming loads compared to GWM. In order to improve 2-D slamming models, a 3-D correction coefficient should be used in the future. The coefficient might be related with a shape and a forward speed.

5. Conclusions

Three different structural models combined with the 3-D Rankine panel method have been tested in the study. The findings from the study are as follows:

Irrespective of the structure modeling method, when a ship structure is correctly modeled, eigenvalue analysis results and responses in waves are confirmed to be almost identical.

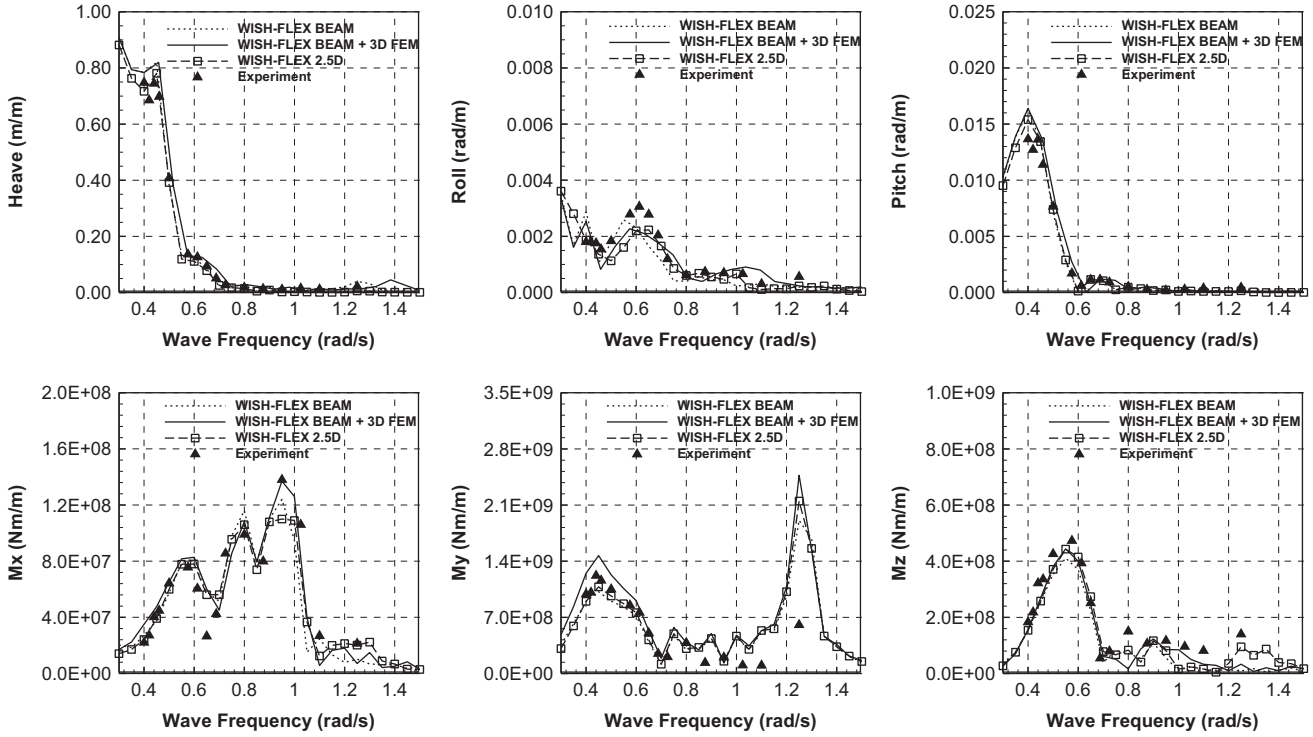

Fig. 26. RAOs of rigid body motions at the mass center and sectional forces at the mid-ship section in oblique seas (linear, 20 knots forward speed, 150° heading angle).

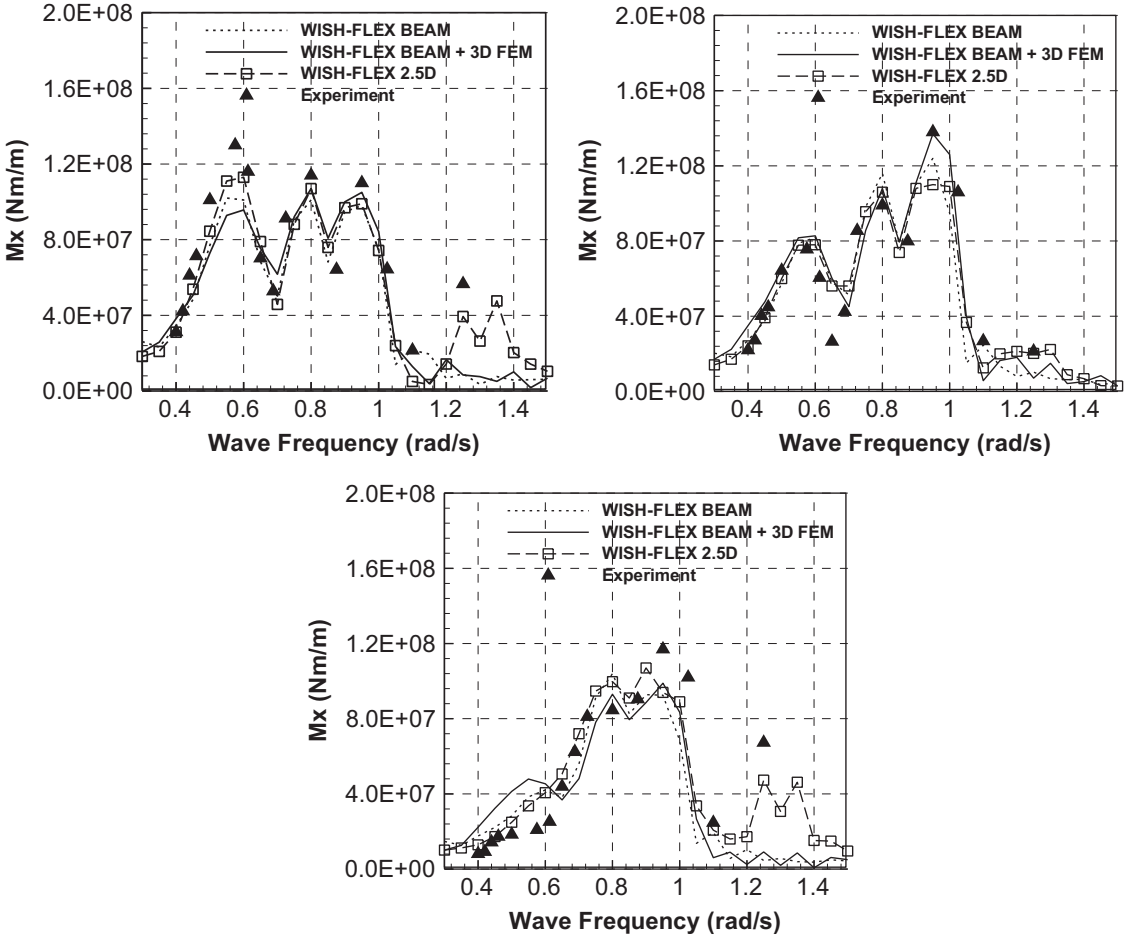

Fig. 27. RAOs of torsional moments at 0.33 (left), 0.50 (middle) and 0.66 L (right) from the AP in oblique seas (linear, 20 knots forward speed, 150° heading angle).

Non-uniform torsion theory in conjunction with consideration of structural discontinuity gives good agreement with the 3-D FE model.

Table 11
Regular wave conditions for nonlinear springing.

Type	Frequency	T (s)	H (m)	Heading (deg)	Speed (knots)
2nd Harmonic Tor.	$2\omega_e = \omega_{tn}$	10.4	5.0	150	17.5
3rd Harmonic Tor.	$3\omega_e = \omega_{tn}$	14.1	5.0	150	18.0
2nd Harmonic V.B.	$2\omega_e = \omega_{bn}$	8.2	5.0	180	19.0
3rd Harmonic V.B.	$3\omega_e = \omega_{bn}$	10.9	5.0	180	18.5

However, the 3-D FE model is rather simple compared to the beam theory model because the beam model is not accurate without additional analysis of the cross-section.

The modified beam model is quite effective to represent modal motion responses of the shell 3-D model but shows over-estimated structural responses in some cases due to the inconsistency between the mass model and eigenvectors.

The 3-D Rankine panel method with weakly nonlinear approach gives good linear responses and reasonable nonlinear springing responses compared to the experiment of 10,000 TEU containership.

2-D GWM and wedge approximation calculate reasonable whipping responses to regular waves, but the methods tend to overestimate whipping compared to the experiment.

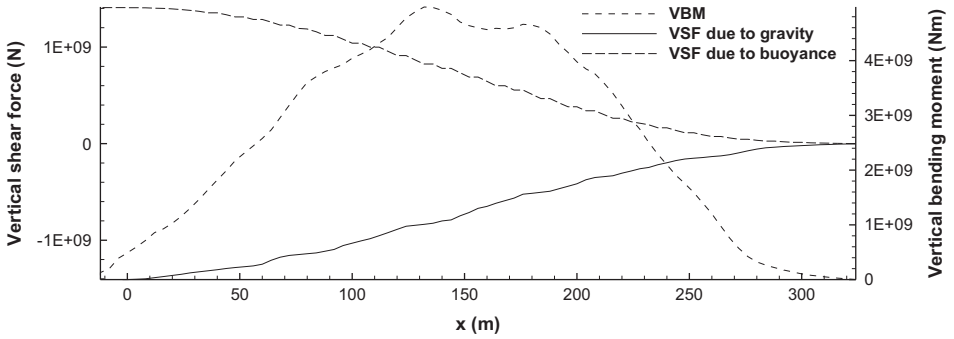

Fig. 28. Longitudinal distribution of still water loads acting on the 10,000 TEU containership

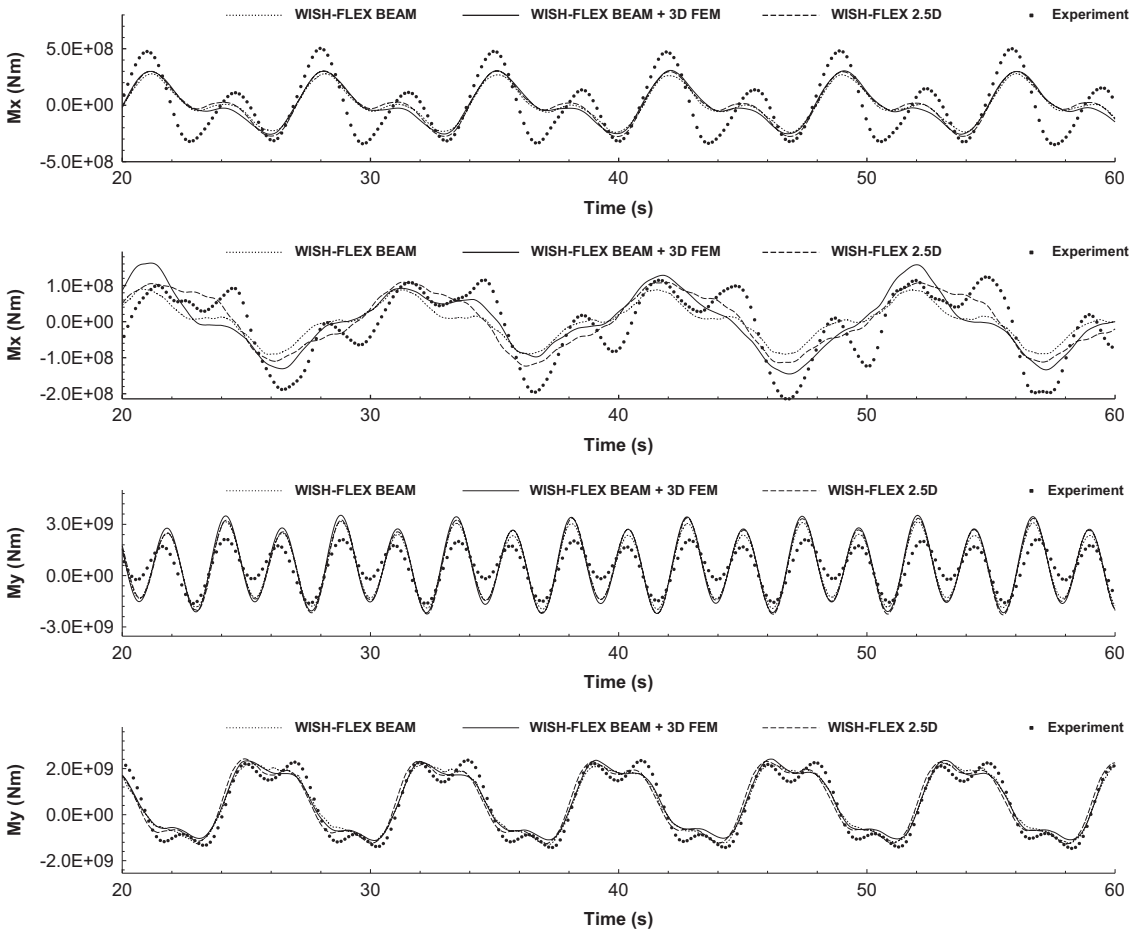

Fig. 29. Super harmonic springing responses: 2nd harmonic of 2-node torsion, 3rd harmonic of 2-node torsion, 2nd harmonic of 2-node vertical bending, and 3rd harmonic of 2-node vertical bending (from top to bottom).

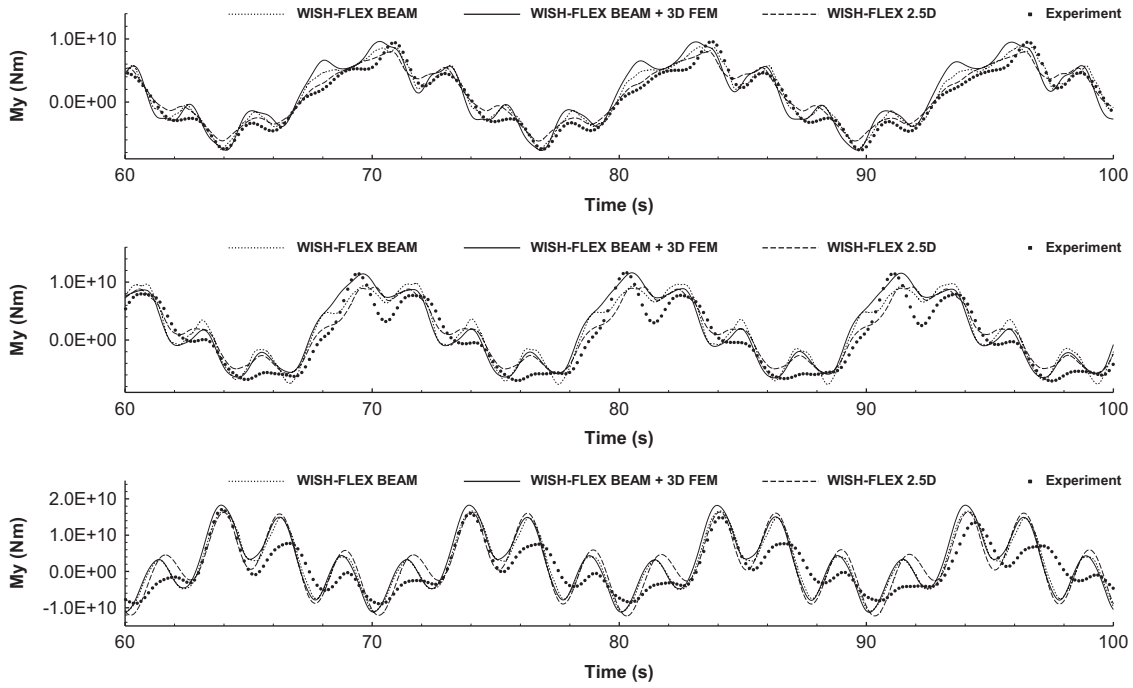

Fig. 30. Whipping responses by GWM in regular waves with different forward speeds: 5 knots; 13.5 knots and 20.3 knots (from top to bottom).

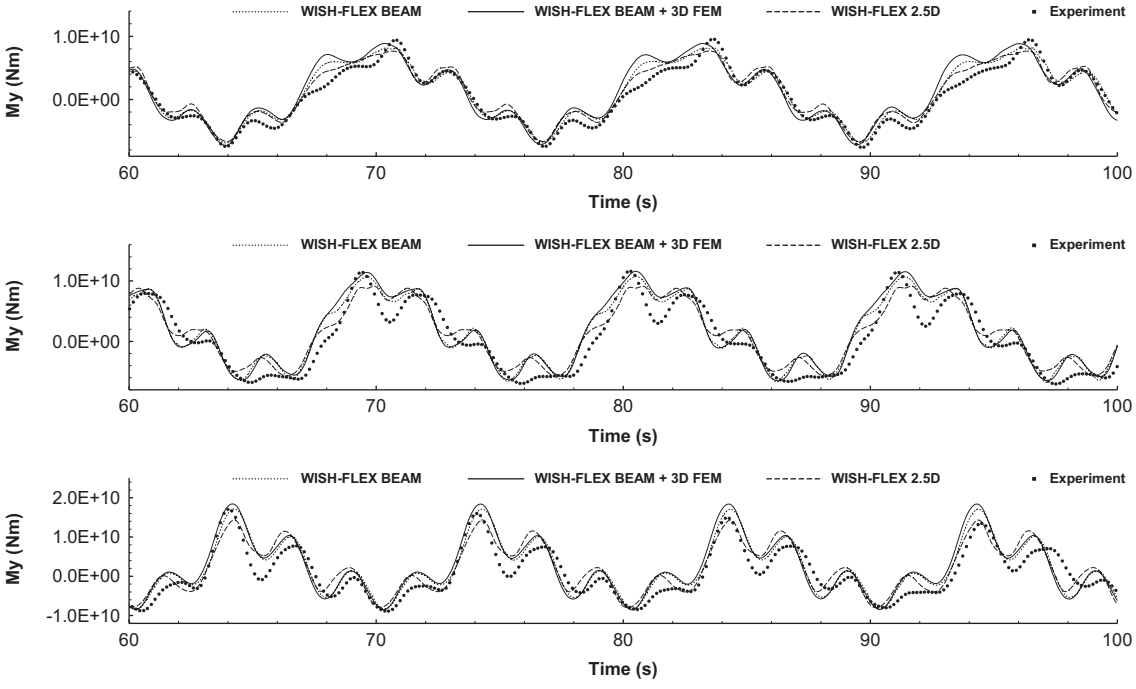

Fig. 31. Whipping responses by wedge approximation in regular waves with different forward speeds: 5 knots; 13.5 knots and 20.3 knots (from top to bottom).

Acknowledgment

This study has been carried out as a part of a project funded by the Lloyd's Register Foundation-Funded Research Center at SNU for Fluid–Structure Interaction, and as a part of WISH-FLEX JIP funded by Daewoo Shipbuilding & Marine Engineering, Hyundai Heavy Industries, Korean Register of Shipping, Samsung Heavy Industries, and STX Offshore & Shipbuilding. Their support is acknowledged. The administrative support of RIMSE and ERI of Seoul National University is also acknowledged.

References

Bigot, F., Derbanne, Q., Sireta, F.X., Malenica, S., 2011. Global hydroelastic ship response comparison of numerical model and WILS model tests. In: Proceedings of the 21st International Society of Offshore and Polar Engineering Conference. US.

Bishop, R.E.D., Price, W.G., 1979. Hydroelasticity of Ships. Cambridge University Press, London.

Dawson, C.W., 1977. A practical computer method for solving ship-wave problems. In: Proceedings of the 2nd International Conference on Numerical Ship Hydrodynamics.

Drummen, I., Storhaug, G., Moan, T., 2008. Experimental and numerical investigation of fatigue damage due to wave-induced vibrations in a containership in head seas. J. Mar. Sci. Technol. 13, 428–445.

Fujitani, Y., 1991. Thin-Walled Beam Structural Analysis. Baihukan Book Company, Tokyo (in Japanese).
Gjelsvik, A., 1981. The Theory of Thin Walled Bars. John Wiley & Sons, New York.
Hirdaris, S.E., Price, W.G., Temarel, P., 2003. Two- and three-dimensional hydroelastic modeling of a bulker in regular waves. Mar. Struct. 16, 627–658.
Iijima, K., Yao, T., Moan, T., 2008. Structural response of a ship in severe seas considering global hydroelastic vibrations. Mar. Struct. 21, 420–445.
Iron, B.M., Tuck, R.C., 1969. A version of the Aitken accelerator for computer interaction. Int. J. Numer. Methods Eng. 1, 275–277.
Jensen, J.J., Dogliani, M., 1996. Wave-induced ship hull vibrations in stochastic seaways. Mar. Struct. 9, 353–387.
Kawai, T., 1973. The application of finite element methods to ship structures. Comput. Struct. 3 (5), 1175–1194.
Khabakhpasheva, T.I., Kim, Y., Korobkin, A.A., 2014. Generalized Wagner model of water impact by numerical conformal mapping. Appl. Ocean Res. 44, 29–38.
Kim, K.H., Kim, Y., 2008. On technical issues in the analysis of nonlinear ship motion and structural loads in waves by a time-domain Rankine panel method. In: Proceedings of the 23rd International Workshop on Water Waves & Floating Bodies. IWWWFB23, Jeju, Korea.
Kim, K.H., Bang, J.S., Kim, J.H., Kim, Y., Kim, S.J., Kim, Y., 2013. Fully coupled BEM–FEM analysis for ship hydroelasticity in waves. Mar. Struct. 33, 71–99.
Kim, Y., Kim, K.H., Kim, J.H., Kim, T., Seo, M.G., Kim, Y., 2011. Time-domain analysis of nonlinear motion responses and structural loads on ships and offshore structures: development of WISH programs. Int. J. Nav. Archit. Ocean Eng. 3, 37–52.
Kim, Y., Kim, K.H., Kim, Y., 2009a. Time domain springing analysis on a floating barge under oblique wave. J. Mar. Sci. Technol. 14, 451–468.
Kim, Y., Kim, K.H., Kim, Y., 2009b. Analysis of hydroelasticity of floating ship-like structures in time domain using a fully coupled hybrid BEM–FEM. J. Ship Res. 53 (1), 31–47.
Kim, Y., Kim, K.H., Kim, Y., 2009c. Springing analysis of seagoing vessel using fully coupled BEM–FEM in the time domain. Ocean Eng. 36, 785–796.
Kring, D.C., 1994. Time Domain Ship Motions by a Three-dimensional Rankine Panel Method (Ph.D. dissertation). Massachusetts Institute of Technology, USA.
Korobkin, A.A., 2010. Mathematics of slamming. In: Proceedings of the 28th Symposium on Naval Hydrodynamics. Pasadena, CA.
Malenica, S., Tuitman, J.T., 2008. 3D FEM–3D BEM model for springing and whipping analysis of ships. In: Proceedings of the International Conference on Design and Operation of Containerships. London.
Maritime and Ocean Engineering Research Institute/Korea Ocean Research and Development Institute (MOERI/KORDI), 2010. Wave Induced Loads on Ships Joint Industry Project-II Report. MOERI Report No. BSPIS503A-2207-2, Korea.
Nakos, D.E., 1990. Ship Wave Patterns and Motions by a Three Dimensional Rankine Panel Method (Ph.D. dissertation). Massachusetts Institute of Technology, USA.
Newmark, N.M., 1959. A method of computation for structural dynamics. J. Eng. Mech. 85 (EM3), 67–94.
Oberhagemann, J., Moctar, O., 2011. Numerical and experimental investigations of whipping and springing of ship structures. In: Proceedings of the 21st International Society of Offshore and Polar Engineering Conference. US.
Ogilvie, T.F., Tuck, E.O., 1969. A Rational Strip Theory for Ship Motions, Part 1. Technical Report 013. Department of Naval Architecture and Marine Engineering, The University of Michigan.
Senjanović, I., Tomić, M., Tomašević, S., 2008. An explicit formulation for restoring stiffness and its performance in ship hydroelasticity. Ocean Eng. 35, 1322–1338.
Senjanović, I., Tomašević, S., Vladmir, N., 2009a. Theory of thin-walled girders with application to ship vibration. Mar. Struct. 22, 387–437.
Senjanović, I., Tomašević, S., Rudan, S., Senjanović, T., 2009b. Role of transverse bulkheads in hull stiffness of large containerships. Eng. Struct. 30 (9), 2492–2509.
Senjanović, I., Hadzić, N., Bigot, F., 2013. Finite element formulation of different restoring stiffness issues in the ship hydroelastic analysis and their influence on response. Ocean Eng. 59, 198–213.
Shao, Y.L., Faltinsen, O.M., 2010. Use of body-fixed coordinate system in analysis of weakly nonlinear wave-body problems. Appl. Ocean Res. 32, 20–33.
Storhaug, G., 2007. Experimental Investigation of Wave Induced Vibrations Increasing Fatigue Damage in Ships (Ph.D. dissertation). Norwegian University of Science and Technology, Tronheim, Norway.
Timman, R., Newman, J.N., 1962. The coupled damping coefficients of a symmetric ship. J. Ship Res. 5 (4), 1–7.
Wu, M.K., Hermundstad, O.A., 2002. Time-domain simulation of wave-induced nonlinear motions and loads and its applications in ship design. Mar. Struct. 15, 461–597.
Wu, M.K., Moan, T., 2005. Efficient calculation of wave-induced ship responses considering structural dynamic effects. Appl. Ocean Res. 27, 81–96.
Zhao, R., Faltinsen, O., 1993. Water entry of two-dimensional bodies. J. Fluid Mech. 246, 593–612.